Your file Votre référence
ISBN: 0-612-83424-7
Our file Notre référence
ISBN: 0-612-83424-7

THIN GOLD FILMS GROWN IN ULTRA HIGH VACUUM ON MICA SUBSTRATES

by

Laura Rezlescu ©

ABSTRACT

In-situ evaporation was used to deposit thin gold films (640 Å) on mica substrates held at room temperature. The samples were characterized by Auger Electron Spectroscopy (AES) and Scanning Tunneling Microscopy (STM) measurements. The deposition of gold on mica without pre-anneal of the mica substrate resulted in a grainy surface with an average grain size of ~220 Å. The evolution of the average grain size as a function of mica pre-deposition baking time and deposition rate was investigated. It was found that long bake-outs (48 hours or more), and low deposition rates (0.2 Å/s) increased the average dimension of gold grains by a factor of 5 relative to the films evaporated onto unannealed mica.

Post-annealing a film deposited at room temperature promoted grain enlargement and enhanced (111) termination. The thermal annealing treatments were done at temperatures between 80 and 340°C, and for periods of time ranging from 1 to 12 hours. In addition to prolonged annealing, *in-situ* flash annealing produced surfaces with highly crystalline terraces extending for as much as 5000 Å. Flashing experiments were carried out at temperatures between 300 and 650°C. Below 350°C, flash annealed and as-grown films were visually similar.

TABLE OF CONTENTS

ACKNOWLEDGMENTS

I am grateful to my supervisor Mark Gallagher, and my family for their support.

This thesis is dedicated to my daughter Catrina.

1. INTRODUCTION

The oriented overgrowth (epitaxy) of vapor deposits on single crystal substrates has captured the interest of thin film and surface physics researchers for a long time. For the surface physicist, the basic mechanisms of epitaxy are intriguing because they reflect in a particularly obvious way the interaction between the surface and the depositing atoms. For the user of thin films, single-crystalline deposits have better defined and often more desirable electrical, mechanical, or optical properties, compared to bulk (Poppa et al., 1970).

With the advent of the Scanning Tunneling Microscope (STM), the interest in the deposition of smooth, well-oriented metal films was renewed (deRose et al., 1991, Golan et al., 1992, Porath et al., 1994). This relatively new tool is particularly useful in studying epitaxy, because unlike many surface techniques which are diffraction based, STM is a real space probe. As a result it can focus on aperiodic features on the surface, helpful in describing the growth process. Information obtained from the STM images includes the shape, size and orientation of the various crystallite domains that constitute the film, the grain boundaries between the crystallites, and surface defects. One of STMs greatest advantages is that it functions not only in vacuum, but also in air and liquids.

The present thesis was motivated primarily by the need to find convenient, flat substrates on which self-assembled monolayers (SAMs) can be observed with the STM. Previous STM studies of gold, ranging from work in both UHV and air on single crystals, to work on Au(111) facets and on Au films grown on mica (Emch et al., 1989) demonstrated that the surface of gold appears to have the characteristics of a suitable SAM substrate. Of all the above surface

preparations, gold in the form of a thin film is the most suitable, because films are easier to shape to fit the needs of an experiment, and far less expensive to grow than bulk crystals. We were interested in gold films firstly because this surface is stable in air, and secondly, because it is the substrate of choice for the growth of thiols (Dishner et al, 1997). Mica was chosen as substrate material for gold films due to its clean and defect-free surface after cleavage. An atomically flat surface is needed, because the topography of the substrate is reproduced in the thin gold film.

When deposition conditions are properly tuned, the gold surface is atomically flat over square micrometers, and consists of very large flat terraces (Holland-Moritz et al., 1991). This almost ideal behaviour of gold on mica made it the subject of several detailed epitaxial studies. Pashley (1956) reviewed the epitaxial growth of fcc metals on mica substrates, and discovered that these films grow in a mixture of orientations that are temperature dependent. However, the texture with the (111) plane parallel to the substrate is dominant.

Poppa et al. (1970) reported a detailed investigation of the epitaxial deposition of gold on mica under well-defined deposition and substrate surface conditions. In addition to the expected (111) termination, they also found evidence of a (211) termination present in small regions of the surface.

X-ray diffraction studies by Reichelt and Lutz (1971) confirmed the existence of two possible in-plane directions for gold grown epitaxially on mica. In the case of room temperature deposition, orientations in which the gold $<1\bar{1}0>$ direction was parallel to both the mica $<0\bar{1}\bar{1}0>$ and $<0\bar{1}10>$ directions were observed.

A wide variety of papers concentrating on STM imaging of gold films have been published over the years. Salmeron et al. (1987) studied gold evaporated onto mica at high temperature, and reported an atomically smooth surface over regions thousands of Ångströms wide, combined with areas consisting of occasional bumps, a few tens of Ångströms high.

Hallmark et al. (1987) applied the STM for in air characterization of 250 nm thick gold epitaxial films on cleaved mica substrates. Their most significant result was the observation of atomic corrugation on the Au(111) surface.

Chidsey et al (1988) studied the influence of the substrate temperature on the epitaxial growth of gold films on mica. With increasing substrate temperature (up to 300°C), the STM images disclosed a topography with larger crystallites having flatter tops, instead of the "rolling-hill" topography seen at room temperature.

Vancea et al. (1989) published a comprehensive study of gold deposited at high temperature onto various substrates. They concluded gold on mica is a "mixed surface" with atomically smooth terraces extending for 600 to 1000 Å, as well as polycrystalline hillocks a few tens of Å high.

In some of the studies, the deposition was followed by a thermal-annealing step. Understanding this step is of practical interest. For example, in the process of fabricating micro-electronic devices, thermal annealing may follow a metallization step, and can affect the physical properties of the metallization layers (Porath et al., 1994). Vries (1987), Chidsey (1988), and later Watanabe (1991) examined the effect of annealing on gold films deposited at room temperature, reporting that annealing has the effect of improving the smoothness of the films,

approaching the morphology of the samples deposited at higher temperatures, but with a much better epitaxial quality. The surface after annealing consisted of flat (111) surfaces with steps and deep valleys.

Several authors proposed different procedures for obtaining the highest quality gold films on mica. In 1991, deRose et al. published the results of their quest for the optimal conditions for large area, flat faces, in gold grown epitaxially on mica: long bake-outs (6 h or more) of the cleaved mica before evaporation and a deposition temperature of 500°C. A popular method to greatly increase the flat surface area (by a factor of 25) is the flame anneal: gold films deposited on high temperature mica are flame annealed in air with a butane torch (Dishner et al., 1998).

We used the results of these previous studies to find the optimal conditions to grow the highest quality Au thin films in our lab. One constraint we had was that all evaporation had to be performed onto room temperature substrates.

The first section of this thesis introduces the reader to the fundamental topics in epitaxy, as they apply to the gold on mica system, and the structure of the Au(111) surface used for this study. The following sections provide detailed information on the experimental techniques and instrumentation used for the preparation and analysis of gold films. The results of the research and their interpretation are presented followed by conclusions.

2. THE NUCLEATION, GROWTH AND EPITAXY OF THIN FILMS

2.1. Introduction

Thin films have always attracted much interest. For a long time they have been technologically important as optical coatings, in corrosion protection and, especially, semiconductor devices. Many of these applications involve increasingly complex growth processes for semiconducting devices. Thin films are also important within physical science itself in exploring differences between three- and two-dimensional states of matter (Venables et al., 1984).

Thin surface films can be prepared by a wide variety of techniques, of which perhaps the most widely used is the evaporation method. It involves condensing the deposit onto a substrate from a vapor. The vapor is produced by thermal evaporation (Campbell, 1966).

The structure (monocrystalline or polycrystalline) of thin films depends on a large number of factors. For metal films produced by thermal evaporation such factors are (Witt, 1974):

- Pressure and nature of the residual gas in the deposition chamber;
- Temperature of the evaporation source;
- Nature of the substrate;
- Temperature of the substrate;
- Surface mobility of deposit atoms on the substrate;
- Presence of charged particles at or near the substrate surface;
- Presence of electric or magnetic fields at the substrate surface;
- Chemical reactions between the deposit and the substrate.

Of major importance in modern technology (especially in the microelectronics industry) are epitaxial films that have been grown on crystalline materials (Lüth, 1993). By definition *epitaxy* is the growth of an oriented single-crystal film upon a single-crystal substrate (Royer, 1928). The phenomenon is called *homeoepitaxy* when the overlayer is the same material as the substrate and *heteroepitaxy* when they are different. According to Van der Merwe (1984), epitaxy owes its technological importance to its unique role in the fabrication of single crystals with certain desired properties.

Royer (1928) was the first to systematically investigate epitaxy. Further progress was slow until UHV techniques for growth and characterization were developed. By using UHV systems (UHV is generally regarded as the vacuum region below 10^{-9} Torr), the detrimental effect of gaseous impurities such as oxygen, nitrogen and hydrocarbons can be reduced (van der Merwe, 1984).

In this chapter we give an overview of the essential factors involved in epitaxy, as it relates to the gold on mica system, and then focus on the structure of gold films.

2.2. Growth modes, processes and kinetics

It is generally accepted that there are three markedly different modes of crystal growth on a substrate surface. These modes of crystal growth (schematically illustrated in fig. 2.1) are named after investigators associated with their initial description.

In the Frank van der Merwe (FM) or *layer-by-layer* mode, the first atoms to condense form a complete monolayer on the surface. Each new layer starts to grow only when the last one has been completed. The interaction between substrate and layer atoms is stronger than that between neighboring layer atoms (Lüth, 1993). This growth mode is observed in the case of adsorbed gases, such as rare gases on graphite and metals, some metal-metal systems, and in semiconductor growth on semiconductors (Venables et al., 1984).

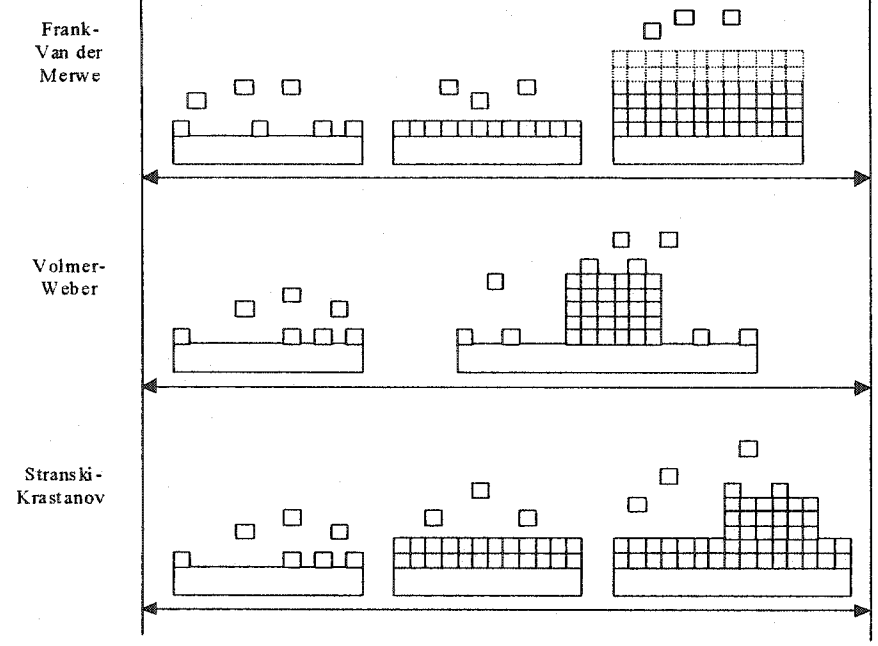

Figure 2.1. Schematic view of the three topologically distinct growth modes (from Zangwill, 1988)

In the Volmer-Weber (VW), or *island* growth mode, small clusters of deposit are nucleated directly on the substrate surface which then grow into islands of the

condensed phase (Venables et al., 1984). This occurs when the interaction between neighboring atoms exceeds the overlayer substrate interaction (Lüth, 1993). This mode is characteristic of metals growing on insulators, including many metals on alkali halides, graphite and other layered compounds. Gold on mica, the system of interest to the present study grows in this mode under certain conditions.

The Stranski-Krastanov (SK) or *layer-plus-island* growth mode is an intermediate case between island and layer growth. After formation of one, or sometimes several complete layers, island formation occurs. Further deposition leads to three-dimensional (3D) islanding. The layer plus island mode is widespread and displayed by many metal-metal, metal-semiconductor, gas-metal and gas-layered compound systems.

*

Let us consider the underlying atomic processes involved in the various growth modes. Thin films are formed on a substrate through nucleation and subsequent growth stages. The stages of transition from individual adatoms to film are illustrated in fig. 2.2. The initial stage consists of the nucleation of small clusters (fig.2.2a) from individual atoms diffusing on the substrate surface (Venables and Price, 1975). These initial nuclei "decorate" the substrate and nucleate preferentially at low-energy sites (cleavage steps or dislocations). With time, more clusters are nucleated (fig.2.2b and c), and they grow (fig.2.2d, e and f) and coalesce (fig.2.2g). A continuous film forms (fig.2.2h), and this film thickens with time. Both nucleation and coalescence can happen in parallel.

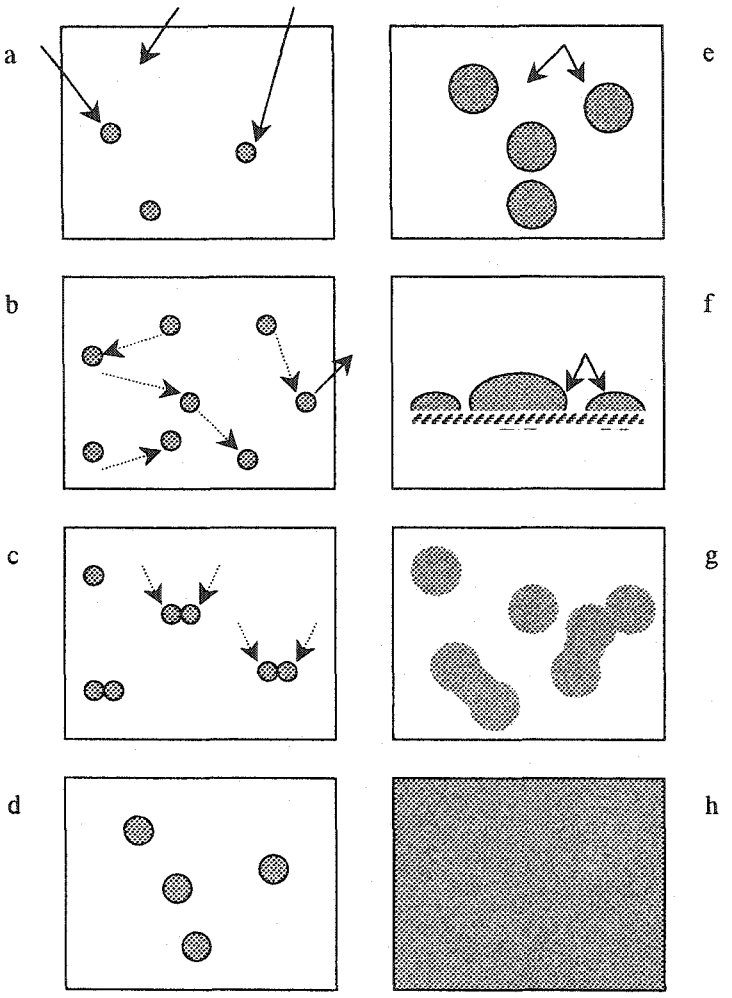

Figure 2.2. Schematic representation of nucleation and growth stages

2.2.f) is a side view of the growing film, as opposed to the rest, which are top view (adapted from Spanulescu, 1975)

Evaporation usually consists of heating the source material to sufficiently high temperatures to yield a vapor. The vapor is commonly modeled as an ideal gas at temperature T_0 and vapor pressure p (van der Merwe, 1984). Using this model the rate at which atoms arrive from the vapor and are accommodated on the surface is given by

$$r = p\,(2\pi MkT_0)^{-1/2} \qquad (2.1)$$

where M is the molecular weight and k is Boltzmann's constant. The population

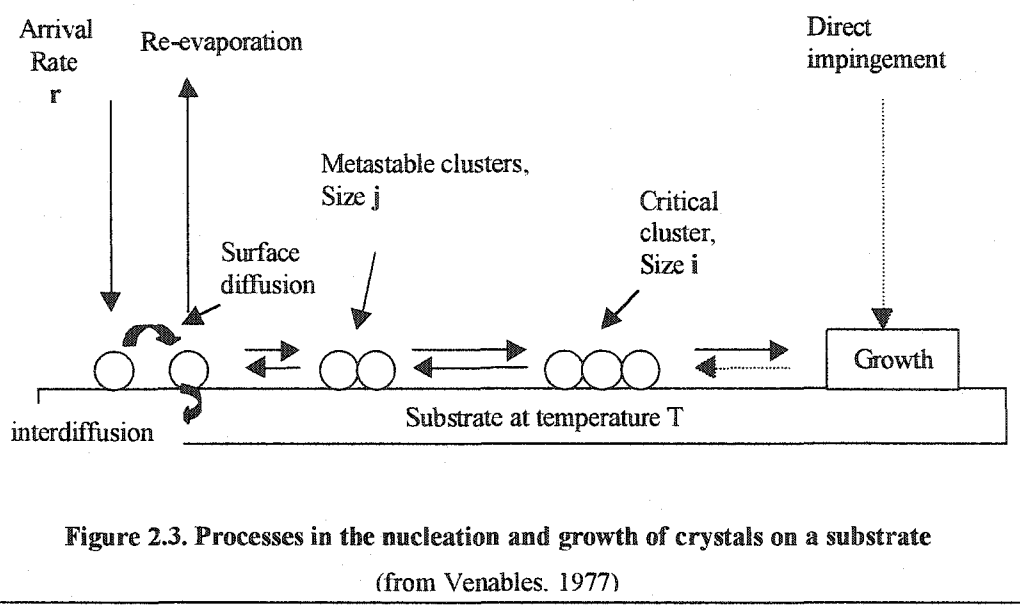

Figure 2.3. Processes in the nucleation and growth of crystals on a substrate (from Venables, 1977)

of single atoms builds up and these atoms diffuse at temperature T, until they are lost by one of the following processes: capture at special defect sites such as steps, nucleation of new clusters, re-evaporation, or possible dissolution into the substrate. On a flat, inert substrate, capture at defects and dissolution can be excluded (Venables et al., 1984) however, real surfaces inevitably contain a distribution of defects which dominate nucleation.

The formation of large, stable clusters is a chain reaction that starts with the formation of small clusters of size j (fig. 2.3), which may decay. Above a certain critical size i, growth is more probable than decay, and these clusters are considered stable. Several processes contribute to growth. Single atoms can diffuse across the substrate to join stable clusters, or they can impinge directly on the growing clusters (fig. 2.3) and become incorporated into them. With these

simple growth processes occurring at the same time as nucleation, the number of stable clusters is increasing. On the other hand, coalescence of two clusters into one decreases the number of stable clusters (Lüth, 1993).

During coalescence, the film particles often exhibit a liquid-phase behavior (Witt, 1974) (fig.2.2g). As a result of coalescence, the compound island usually has a greater thickness than the two initial islands. When islands have a crystallographic profile instead of rounded shapes, coalescence immediately leads to the rounding of the corners of the islands (Pashley, 1965), and a compound island with a very rounded profile is usually formed. The liquid-like coalescence leads to regions around the large compound islands being free from deposit. This immediately results in the formation of secondary nuclei, which coalescence in the same way as the primary nuclei. Eventually these secondary nuclei touch the sides of the larger primary islands, and coalesce in a pronounced liquid-like manner, giving the appearance that the smaller island flow into the larger island (Pashley, 1965). Even though the general coalescence behaviour has been described as liquid-like, the deposit is certainly not liquid, its temperature being well below the melting point.

2.3. Thermodynamic considerations

In thermodynamic equilibrium, all processes discussed proceed in both directions at equal rates, as required by the principle of "detailed balance". For example, surface processes (which take place during nucleation and growth of thin films), such as condensation and re-evaporation, decay and formation of two-

dimensional clusters, must obey detailed balance (Venables et al., 1984). Therefore, in equilibrium, there is no net growth of a film. By contrast, the growth process of a thin film is a non-equilibrium kinetic process (Venables et al., 1984) and the final macroscopic state of the system depends on the route taken through the various reaction paths indicated in fig. 2.3. Generally, certain parts of the overall process may be kinetically forbidden (such as dissolution into the substrate), whereas others may be in "local thermodynamic equilibrium". In this case, equilibrium arguments may be applied locally, even though the whole growth process is a non-equilibrium process.

Thermodynamics makes it possible to predict the growth mode of a deposit. Force equilibrium at the point where the substrate and a 3D island of the deposited film touch (fig. 2.4, Lüth, 1993) requires

$$\gamma_S = \gamma_{S/F} + \gamma_F \cos\phi \,, \qquad (2.2)$$

where γ_S is the surface tension (the characteristic free energy per unit area to

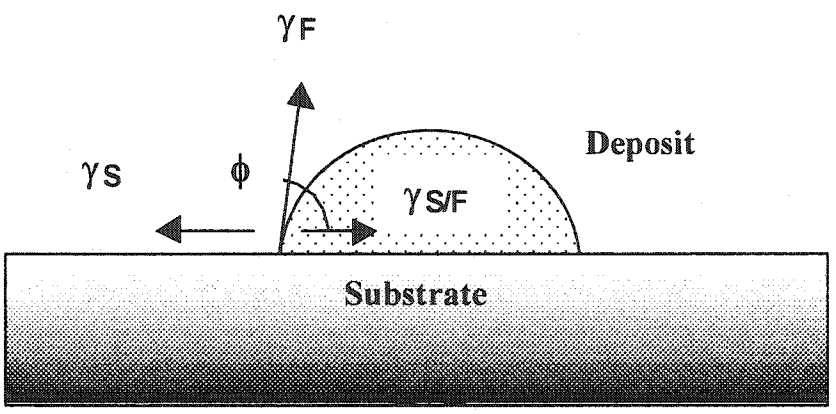

Figure 2.4. Simplified picture of an island of a deposited film

(from Lüth, 1993)

create an additional piece of surface or interface) of the substrate/vacuum interface, γ_F that of the film/vacuum and $\gamma_{S/F}$ that of the substrate/film interface. γ can also be interpreted as a force per unit length of boundary. Using this equation the two limiting growth modes, -layer-by-layer (FM) and island (VW)- can be distinguished as follows (Lüth, 1993):

(1) layer-by-layer (FM) growth: $\gamma_S \geq \gamma_F + \gamma_{S/F}$; (2.3.a)

(2) island (VW) growth: $\gamma_S < \gamma_F + \gamma_{S/F}$. (2.3.b)

The relations (2.3) are not complete if one considers the equilibrium condition for the whole system including the gas phase above the deposited film. Since equilibrium is determined by a minimum of the Gibbs free energy, one has to take into account a contribution $\Delta G=n\Delta\mu$ (n is the particle number, and $\Delta\mu$ is the change in the chemical potential) when a particle is transferred from the gas phase into the condensed phase of the deposited film (Lüth, 1993). If this transfer occurs exactly at the equilibrium vapor pressure $p_0(t)$, then no energy is needed because of the equilibrium condition $\mu_{solid}(p_0,T)= \mu_{vapor}(p_0,T)$. If, however, the particle changes over from vapor to solid at a pressure p, a free energy change:

$$\Delta G=n\Delta\mu=nkT \ln(p/p_0) \quad (2.4)$$

is involved. The ratio p/p_0 is called the "degree of super-saturation" (Lüth, 1993). Taking this vapor phase into consideration, the conditions (2.3) have to be supplemented as follows:

(1) layer-by-layer (FM) growth: $\gamma_S \geq \gamma_F + \gamma_{S/F} + CkT \ln(p_0/p)$ (2.5a)

(2) island (VW) growth: $\gamma_S < \gamma_F + \gamma_{S/F} + CkT \ln(p_0/p)$ (2.5b)

where C is a constant. From the relations above, one sees that the growth mode of a certain material on a substrate is not a constant material parameter, but the growth mode can be changed by varying the super-saturation conditions (i.e., the flux). For example, with increasing super-saturation, layer by layer growth is more favoured.

In the present study, deposition rates varying from 0.2 Å/s to 3 Å/s were used. These deposition rates correspond to a range of degree of super-saturation of between 10^{18}-10^{19}. According to Lüth (1993), this is typical of epitaxial growth of materials with low equilibrium vapor pressure, such as gold.

Estimation of both the critical radius of the clusters, and the concentration of the critical nuclei is also possible using thermodynamics. Both the critical radius of the clusters and the concentration of critical nuclei strongly depend on the nature and the temperature of the substrate, on the degree of super-saturation and on the film-substrate interaction. The size *i* corresponding to the critical cluster (defined as the cluster for which the free energy is maximum) can be determined by maximizing Gibbs free energy of formation of a spherical cluster (Rhodin, 1966):

$$i = -\frac{2\gamma_F}{\Delta G_V}, \qquad (2.6)$$

were γ_F is the interfacial free energy per unit area of the film/vapor interface and ΔG_V is the Gibbs free energy change per unit volume associated with the transformation of the adsorbed atom to the cluster.

Experimentally it is found that for most metal systems the critical nucleus is just 1 or even 0 atoms.

2.4. Nucleation and epitaxy

It is necessary to remember that epitaxy is the growth of an oriented crystal film upon a single crystal substrate. As already mentioned in section 2.2, the nucleation of a deposited film begins at many different nucleation sites, usually at imperfections in the substrate surface. With increasing individual islands (clusters), coalescence starts and finally results in a continuous film. Provided all islands have the same epitaxial orientation to the substrate, a single crystalline epitaxial film will be formed by island coalescence. On the other hand, if islands with different orientations grow together, a polycrystalline film may result (Wagner, 1988).

There are at least two factors contributing to the formation of oriented crystalline layers (Rhodin, 1966):

a. ***Nucleation orientation***. The occurrence of epitaxy depends on the formation of highly oriented nuclei. A number of good reviews on epitaxy indicate the importance of the orientation of the critical nucleus in the formation of overgrowths with unique structure (Pashley, 1965, Rhodin, 1966, Adamsky, 1966, Francombe, 1966). Rhodin and Walton (1964) suggest that there are two mechanisms by which a particular orientation may be favoured: (1) the critical nucleus which leads to the final orientation is adsorbed more strongly than any other; (2) the critical nucleus which leads to some other orientation is adsorbed strongly and energetically favored, but subsequent growth of the cluster requires the addition of atoms in unfavorable positions. Thus while a deposit with this orientation may nucleate it does not grow. As an example of the first mechanism,

Cu, Ag and Au grown on NaCl (100) have a (100) termination, and the in plane [110] direction is parallel to the [110] direction of the substrate. This so-called "parallel" orientation occurs despite a large 27% misfit between deposit and substrate. In fact, rotation by 45 degrees ([110] parallel to the [100] direction of the substrate) would only amount to a misfit of 3%. Therefore the final orientation of the deposit is determined by the stronger initial nucleation of [110] grains, despite the large misfit.

b. ***Orientation changes and recrystallization***. Although one could consider that perfect epitaxy occurs as a result of the formation of nuclei aligned exactly in the same orientation on a single crystal substrate, electron diffraction evidence indicates that epitaxy can occur even when the initial nuclei are poorly oriented. This means that a transition occurs in the film after initial nucleation and growth to a state of lower free energy. It was found experimentally that the nuclei of gold on molybdenite (Pashley et al., 1964), and silver on mica (Matthews, 1962) tend to rotate slightly during growth, particularly during coalescence, when slightly misaligned nuclei were observed to rotate into perfect alignment. The rotation effect explains how the orientation of a deposit can improve as it becomes thicker (Pashley, 1965).

The appreciable orientation changes that occur during the growth stages have an important effect on the nature and quality of epitaxy present in a continuous film. This is highlighted by the evidence of Matthews (1965) that the controlling process in the epitaxy of metals on rocksalt is that of recrystallization during coalescence of nuclei and islands. Thus from the point of view of epitaxy the

orientation changes are of two important kinds, (Pashley, 1965): (1) improvement in the alignment of nuclei and islands as growth proceeds; or (2) preferential growth of nuclei and islands of one preferred orientation at the expense of nuclei and islands in another preferred orientation.

It is experimentally found that for the gold on mica system, the dominant termination is (111) parallel to (001) plane of the mica. Two possible in-plane directions were reported in the case of room temperature deposition: the gold $<1\bar{1}0>$ parallel to the mica $<010>$, and the gold $<\bar{1}\bar{1}0>$ parallel to $<0\bar{1}0>$ of the mica. At higher substrate temperatures, the former orientation prevails.

In first orientation, the rows of gold atoms are parallel to the rows of oxygen and potassium atoms. The misfit parameter is defined as the ratio f = (a-b)/a, where a is the lattice spacing of the film, and b is the lattice spacing of the substrate (Zangwill, 1988), and has a relatively large value for this orientation, of 11% (Chidsey et al., 1988). This has been calculated taking into account a gold nearest-neighbour spacing of 2.88 Å along the $<1\bar{1}0>$ direction and a nearest-neighbour spacing of 2.56 Å for the oxygen atoms along the mica $<010>$ direction. The much smaller misfit (only 3%) in the second in-plane orientation is due to a value of 2.79 Å for the mica nearest-neighbour spacing along the $<0\bar{1}0>$ direction, which is much closer to the 2.88 Å lattice spacing for gold along the $<1\bar{1}0>$ direction.

The large epitaxial misfit, combined with a degree of super-saturation in the range of 10^{18}-10^{19}, and the fact that gold has a greater surface energy compared

to mica (~1J/m^2 for gold (Venables, 2000) as opposed to 0.38 J/m^2 for mica (Hazen et al., 1981)) lead to a thermodynamically predicted island growth mode for the epitaxial system at hand (Au on mica).

The structure of the Au(111) surface will be discussed in paragraph 2.6.

2.5. Conditions for the occurrence of epitaxy

In order to obtain well-defined epitaxy, it is necessary to control the deposition conditions. Some of the most important variables are: 1) substrate temperature; 2) rate of deposition; 3) substrate preparation; and 4) deposit thickness (Pashley, 1965).

1) Some of the most systematic evidence exists for the effect of substrate temperature, as first examined carefully by Bruck (1936). He showed that for the growth of fcc metals on rocksalt, there is a critical substrate temperature above which he obtained good quality epitaxy and below which epitaxy did not occur. Many workers repeated Bruck's experiments and found different values for this critical substrate temperature. It is therefore clear that other deposition variables also have an important influence. The general conclusion, however, is that increasing the substrate temperature influences the occurrence of epitaxy in several ways: a) by providing some of the activation energy which is required to allow the deposit atoms to take up position of potential energy minima associated with ordered epitaxy; b) by increasing surface and volume diffusion, which is important for accommodating the misfits which occur as neighboring nuclei grow

together. It is generally not possible to define a precise value for the critical substrate temperature, since several independent factors are involved, and these are influenced by other deposition conditions (Pashley, 1965).

2) It was also found experimentally that the rate of deposition (degree of super-saturation) influences the occurrence of epitaxy. As a general rule, the slower the deposition rate, the more likely is epitaxy to occur, if epitaxy is thermodynamically favored.

3) The preparation of the substrate surface is important for at least two reasons: first, the topography, or micro-geometry of the surface has a direct influence on the orientation of the deposit. The other major influence is the cleanliness of the substrate surface. In some cases, exposure to air is enough to cause significant changes. The first evidence in this regard was obtained by Ino et al. (1962). They cleaved heated NaCl crystals inside the vacuum system 10^{-4}-10^{-5} Torr), with the evaporation source already emitting, so that deposition commenced immediately after cleavage. By repeating the experiment at different temperatures, and comparing the results with those obtained by simultaneously depositing on specimens previously cleaved in air, they determined the effect of the air exposure on the substrate temperature. For a constant evaporation rate (10-50 Å/min), and a film thickness of 400-500 Å, it was found that for Au, Cu and Ag deposits the critical substrate temperature for epitaxy is much lower for cleavage in vacuum. The same authors (Ino et al., 1962) improved the vacuum to 10^{-7}-10^{-9} Torr, in order to reduce the amount of substrate contamination which can occur as the film is being deposited. It was then found that whereas cleavage in the

ordinary vacuum lowered the critical temperature for Au, Cu and Ag, cleavage in the UHV resulted in a deterioration of the parallel orientation. This indicates that a certain amount of contamination can be beneficial in bringing about epitaxy, and it stresses the importance of determining the role of various types of contaminants on the growth mechanism of thin films.

The systematic study conducted by Harsdorff and Raether (1964) on the growth of silver on rocksalt crystals cleaved in vacuum (10^{-4}-10^{-6} Torr) confirmed the above findings. Specifically, their results provided evidence that the perfection of epitaxy depends on the time interval between cleavage and deposition of silver, and the better the vacuum the slower must be the rate of deposition if good epitaxy is to be obtained. The latter result could be interpreted as meaning that less contamination at the surface leads to smaller density of nucleation sites. Thus a slow rate of deposition must be used in the cleaner vacuum to allow sufficient time for the adatoms to diffuse further on the surface to reach stable sites.

4) The orientation in a thin deposit film can change appreciably with deposit thickness. There is some systematic evidence supporting the idea that in certain systems, the orientation in the deposit improves considerably with further deposition. The growth of silver on mica provides a clear example: it was found by Matthews (1962) that the nuclei of silver tend to rotate slightly (by angles of 1 or 2 degrees) during growth, particularly during coalescence when two slightly misaligned nuclei were observed to rotate into perfect alignment. This rotation

effect explains how the orientation of a deposit can improve as it becomes thicker.

2.6. Au(111) and the *herringbone* reconstruction

It is necessary to look now at the structure of Au(111), since this was the surface we studied. Noble metals such as gold arrange themselves in a face-centred

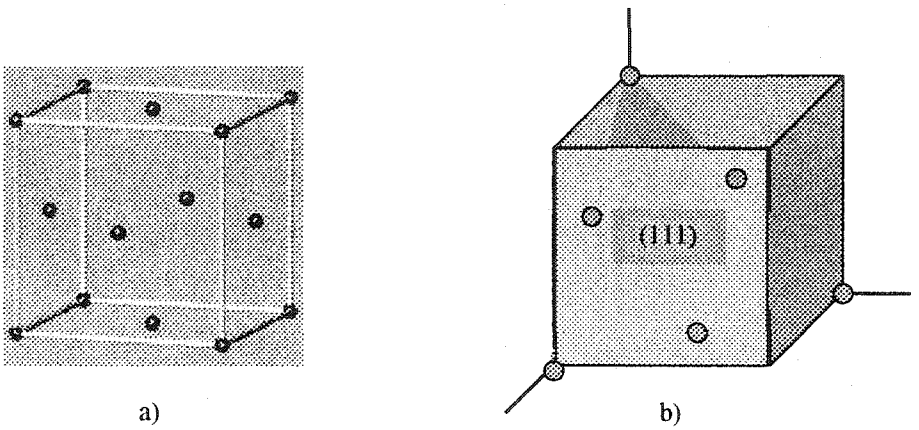

Figure 2.5. a) Unit cell of face centered cubic lattice;
b) (111) plane of the face centered cubic structure
(adapted from Kittel, 1996)

cubic lattice (fig. 2.5a). The conventional unit cell contains four lattice points -at the centre of the faces of the cube and at the vertices, i.e. at (1/2,1/2,0), (0,1/2,1/2), (1/2,0,1/2) and (0,0,0).

In a hard sphere model, the balls in the {111} planes touch their six nearest-neighbours and are known as the close packed planes. The fcc structure is one

of two close packed structures. In the hard sphere model it has a packing density of approximately 74%.

A (111) lattice plane within the face-centered (fcc) Au crystal is a hexagonal array of atoms at positions (0,0,1), (1,0,0), (0,1,0), (0,1/2,1/2), (1/2,0,1/2), (1/2,1/2,0), as shown in fig. 2.5b. If we look at the (111) plane in the unit cell, the three face diagonals form the sides of an equilateral triangle. Using a hard sphere model, the (111) plane of an fcc structure can be regarded as a layer of close-packed spheres as shown in fig. 2.6. From this figure, the fcc structure arises from an ABCABC... stacking sequence of close packed planes.

If the Au(111) surface kept this structure, the flat terraces between atomic steps would appear featureless, however the surface reconstructs. The reconstruction is quite a complex system consisting of both short-range and long-range

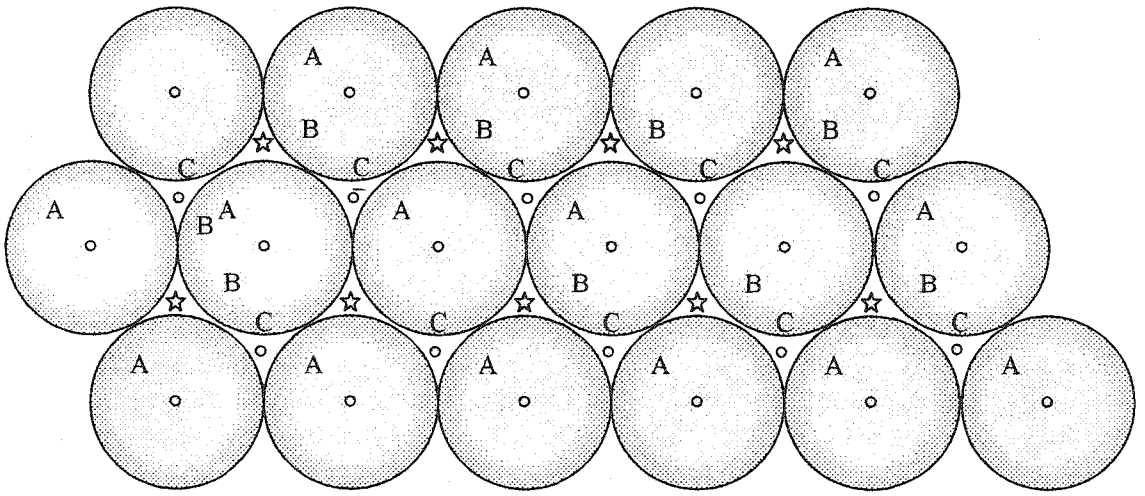

Figure 2.6. A close-packed layer of spheres is shown, with centers at points marked A. A second identical layer of spheres can be placed on top of this, above and parallel to the plane of drawing, with centers over the points marked B. There are two choices for a third layer. It can go in over A or over C. If it goes in over A the sequence is ABABAB... and the structure is hexagonal close packed. If the third layer goes in over C the sequence is ABCABCABC...and the structure is face centered cubic.

(adapted from Kittel, 1996)

structure called the *herringbone* pattern.

The (111) surface undergoes a surface reconstruction to reduce surface energy (to compensate for the smaller number of nearest neighbours, 9 instead of 12 as in the bulk), and results in the top layer of gold atoms adopting a $(22\times\sqrt{3})$ unit cell. A model of the rectangular unit cell is illustrated in fig. 2.7a. The short edge of the unit cell is 4.99 Å long ($\sqrt{3}$ times the gold-gold distance of 2.88 Å) and lies along the next nearest-neighbor direction of gold atoms in the (111) plane. The long edge is 63.36 Å long and is aligned along another nearest- neighbor

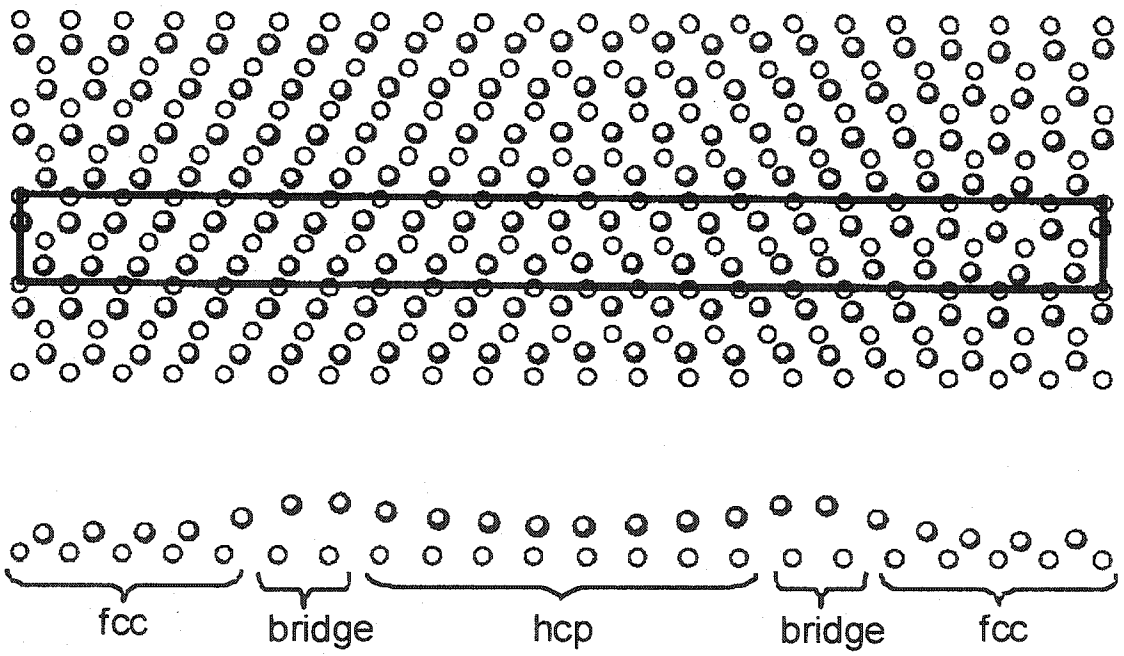

Figure 2.7. a) Schematic representation of the gold $(22\times\sqrt{3})$ reconstruction as see from above; the unit cell is shown by the rectangle, which has dimensions of 63.36 Å × 4.99 Å. The reconstruction stripes that are experimentally observed are the result of stacking these unit cells in the direction of the short axis (i.e., the next-nearest neighbor direction).

b) The same reconstruction but viewed from within the gold surface (i.e., end on). The vertical displacement of gold atoms creates a region that is filled by atoms in hcp sites. (Dishner et al. 1997).

direction. As one travels along the long edge of the unit cell, the environment of the surface gold atoms changes from fcc stacking at one edge, through a transitional period of the so-called "bridging sites" to hcp stacking in the center, and then returns to fcc stacking at the other edge following another bridging transition. The gold atoms in bridging sites have been shown to be vertically displaced by 0.20 Å.

The gold atoms in hcp sites are also vertically displaced with respect to their bulk fcc positions by 0.12 Å. An exaggerated model of the vertical displacement for the reconstruction is depicted in fig. 2.7b (Dishner et al, 1997). With the STM, the reconstruction is seen as straight stripes that tend to zigzag, which is why it is called the "herringbone" reconstruction. One consequence of the reconstruction is a 4.4% increase in the density of atoms in the outermost layer compared to that of atoms in the bulk.

3. EXPERIMENTAL TECHNIQUES AND APPARATUS

3.1. Ultra High Vacuum (UHV)

3.1.1. Introduction

A vacuum is a space from which air or other gases have been removed (O'Hanlon, 1989). However, gas molecules cannot be completely removed from a chamber. The amount of gas to be removed depends on the application of the vacuum. All surface analytical techniques require that the composition of a sample surface remain essentially constant over the duration of an experiment. At atmospheric pressure, molecules are constantly impinging on the surface. These molecules can be either physisorbed or chemisorbed by the surface. Therefore, in order to make an accurate study of a freshly prepared crystal surface, the sample needs to be introduced and prepared in an UHV chamber where it remains clean for long periods of time. According to the kinetic theory of gases, the time to saturate a surface with one layer of molecules, assuming a unity sticking coefficient, is (O'Hanlon, 1989):

$$t=(4kT)/(Pvd_0^2), \qquad (3.1)$$

where P is the ambient gas pressure above the surface, T its thermodynamic temperature, d_0 is the molecular diameter, and v is the average velocity of the molecules. k represents Boltzmann's constant. Equation (3.1) shows that at room temperature and atmospheric pressure, a monolayer of air (d_0=0.372 nm, v=467m/s) will form in about 25 ns, whereas under UHV conditions (UHV is

generally regarded as the region below 10^{-9} Torr), it will take over 5 hours to cover the sample.

All the experiments in the present thesis, with the exception of STM imaging, were carried out in an ultrahigh vacuum system with a base pressure of 2×10^{-10} Torr. The chamber is equipped with a Residual Gas Analyzer (RGA), Auger Electron Spectrometer (AES), and evaporator. A brief description of each of the components that are relevant to this study is given in the following subsections.

3.1.2. Materials for use in UHV

In general, all materials are permeable to gases and release gas when exposed to a vacuum. Despite this difficulty, an appropriate combination of materials can be used to construct a UHV system.

The vacuum chamber and its associated pipework are fabricated of vacuum-braised stainless steel. This material corrodes very slowly and has low outgassing rates. Glass also plays an important role in the construction of the system, for it is the preferred material for windows.

The vacuum joints are made with copper gaskets. Copper offers the advantage that it has almost the same coefficient of thermal expansion as that of stainless steel, which is very useful during bake-out. The use of metal gaskets avoids release of organic contaminants, reduces leakage of water vapor from the atmosphere into the system, and allows the baking of the system.

The materials used inside the vacuum chamber are carefully chosen to avoid high vapor pressures. Stainless steel, molybdenum and tantalum are usually used for fabricating parts, oxygen-free high-conductivity copper is often used as a conductor, and glass and high-density ceramics are used as electrical or thermal insulators.

3.1.3. Vacuum pumps

A vacuum system is a combination of pumps, valves and pipes that creates a region of low pressures (O'Hanlon, 1989). Vacuum pumps can be divided into two classes: pumps that can commence operation at atmospheric pressure, and the second type, pumps that can only function at low pressures. The latter produce a high vacuum and are always used in association with the former, which are known as "backing pumps", as their role is to produce a backing vacuum.

The following pumps were used to evacuate the vacuum chamber in our laboratory: ion pump, titanium sublimation pump, and for initial pumping from atmospheric pressure, turbomolecular pump backed up by rotary vane pump.

The *rotary pump* is used for backing up the turbomolecular pump and for initial chamber evacuation. This pump utilizes a rotor to provide a rotary movement and sweep gas from the chamber, by means of two spring-loaded vanes, to the atmosphere, via an oil-sealed non-return valve (Ferguson, 1989). It has an ultimate pressure of 60 mTorr.

The *turbomolecular pump* is a bladed axial-flow turbine that compresses gas by transfer of momentum (vector) from the high-speed rotating blades of the rotor to the gas molecules. The pump rotor contains a number of slotted disks (sets of rotor blades) which are interposed between fixed disks (sets of stator blades). The angles of the slots in the fixed disks oppose those of the rotating disks. The relative velocity between rotor and stator makes it extremely probable that gas molecules will be transferred from the pump inlet to the exhaust, where the mechanical rotary pump finally exhausts the pumped gas to the atmosphere. Each rotor disk is able to support a differential pressure. Because the compression ratio is small for a single pair of rotating/fixed disks (rotor/stator stage), it is necessary to use a series of stages. The total compression ratio is then the product of the ratios achieved in each stage. Our pump operates at a rotor speed of 70,000 rpm and has a pumping speed of 60 L/s. The ultimate pressure attainable is 1×10^{-9} Torr.

The *titanium sublimation pump* (TSP) is a surface getter pump and it operates by capturing gas molecules and binding them to a surface. Titanium is the material of choice for surface getters because of its low temperature of sublimation, its relatively reduced cost, and its capability of pumping a large number of gases. Titanium is sublimed and deposited on the adjacent walls. The fresh titanium surface captures active gases. A new titanium layer is deposited on a periodic basis in order to ensure continuous pumping. Due to cleanliness, bakeability, low power consumption, vibration-free operation, long pumping life, and high

pumping speed, the Titanium Sublimation Pumping (TSP) is an ideal cost-effective companion to ion pumping in ultrahigh vacuum.

An *ion pump* consists of a parallel array of short stainless steel tubes, two plates (Ti) spaced a short distance from the open ends of the tubes and a strong magnetic field parallel to the tube axes. The principle of operation is very simple: electrons released from the (cathodic) plates are constrained by the magnetic field into tight helical trajectories in the (anodic) tubes. The increased path length increases probability that the electron will collide with a gas molecule and ionize it. The electric field between the anode and cathode accelerates the ions to the cathode where they can be buried. The process also sputters Ti which can act as a getter for active gases. The operating pressure range of a typical ion pump extends from 10^{-2} to 10^{-11} Torr.

All our pumps, with the exception of the mechanical pump, were manufactured by Varian Vacuum Products (Lexington, MA).

3.1.4. Ion gauge

An important component in any vacuum apparatus is the vacuum gauge. For many years, the lack of gauges capable of measuring very low pressures constituted an impediment in the development of UHV technology (Ferguson, 1989). The most commonly used UHV gauges are ionization gauges. These gauges operate based on the fact that, in a diode with stable emission from its cathode and at a given electron energy, the number of ion pairs produced in a

particular gas depends upon the pressure. Consequently, when a high voltage is

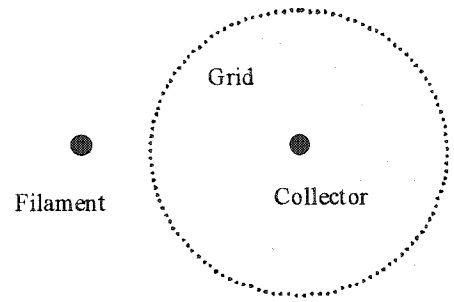

Figure 3.1. Schematic diagram of Bayard-Alpert ion gauge (adapted from http://www.nottingham.ac.uk/~ppzpjm/sect3_4.htm)

used to set up an ionization current in a gas, the current is determined by the total pressure (Ferguson, 1989).

The *Bayard-Alpert* ion gauge (fig.3.1) is basically a triode in which the electrons emitted from a heated filament are accelerated towards a grid held at several hundred volts positive. Some electrons pass through this grid and ionize the residual gas present. The positive ions are collected at a negative plate electrode (collector) and the ion current is amplified and measured.

Our vacuum system is equipped with a Varian's nude Bayard-Alpert gauge, which can operate at pressures of 10^{-11} Torr.

3.1.5 Residual gas analyzer

Often it is important to know not only the pressure in a vacuum but also exactly what residual gases are present. Therefore, the residual gas analyzer (RGA) is

an indispensable instrument in any vacuum system. RGA is the term for a class of quadrupole mass spectrometers that typically cover mass ranges from 1 to 100 or 200 atomic mass units (amu), and are used for the analysis of the gasses present in UHV. It measures the ratio of mass to electric charge of an ion. Basically, the gas molecules are first ionized, then directed through a mass separator, and finally detected (O'Hanlon, 1989).

The most important part of the quadrupole mass analyzer is the mass filter, seen in fig. 3.2. This separates species of different mass to charge ratio and consists of four cylindrical electrodes or poles arranged to occupy the corners of a square.

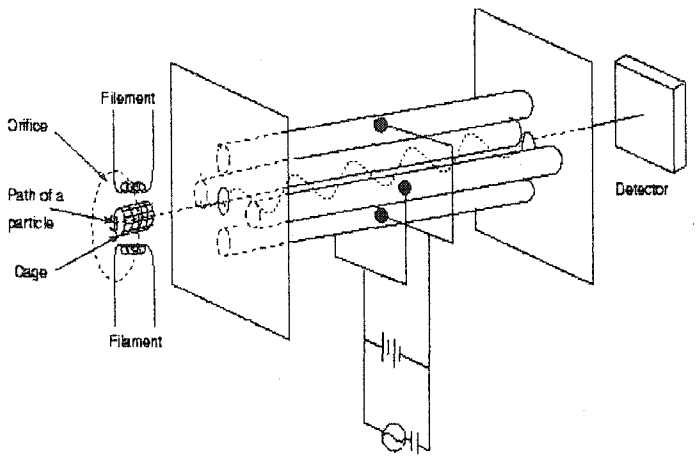

Figure 3.2. Schematic of a quadrupole mass filter (http://www.personal.psu.edu/faculty/r/x/rxj10/research/setup.html)

The diagonally opposite poles are supplied with a RF voltage superimposed on a DC voltage. The other set of poles receive the same supply in opposite polarity. By controlling the potentials and RF frequency, the desired mass can be transmitted through the probe.

The qualitative interpretation of RGA data (mass scans) is straightforward: molecules of a gas are struck by electrons, causing their ionization. This leads to the formation of several mass-to-charge ratios, unique for each gas species. One can use this fingerprint to positively identify a gas or a vapour. We use the RGA to diagnose potential problems in the vacuum chamber, such as pump oil contamination, an air leak, or outgassing from components within the chamber. The RGA's resolution is sufficient to clearly distinguish between peaks that are 1 amu apart.

The RGA in use in our laboratory is an SRS RGA 100 purchased from Stanford Research Systems (Sunnyvale, California). The "100" indicates that our model measures up to 100 amu.

3.1.6. "Baking" the system

10^{-8} Torr is the *ultimate pressure* (defined by Ferguson as the "limiting pressure approached in a vacuum chamber after pumping for sufficient time to establish that any further reduction in pressure will be negligible") attainable with all the vacuum pumps operating. Therefore, an important ingredient in obtaining UHV is the need to bake the whole system (O'Hanlon, 1989).

Normally, a UHV system must be degassed before use. The purpose of this process (known as "baking") is to reduce the outgassing rate of the walls. This is done by first heating the chamber to promote outgassing. After the bake, when

the temperature of the chamber is reduced, the near surface region of the walls is depleted and the room temperature rate is reduced.

The whole chamber assembly is designed so that it can be heated in excess of 400°C, but we are limited by some instruments, such as the AES, and RGA to 125°C while the vacuum pumps operate. In our laboratory, baking is carried out by wrapping the whole vacuum system with electric heating tapes. Aluminium, in the form of domestic kitchen foil, is used as a thermal reflector during bake-out. The "baking" of the system at 125°C for 48 hours results in accelerated desorption of water vapour (and other gases) from all internal surfaces. When the bake ends and the system is cooled back to room temperature, the ultimate pressure attainable is substantially reduced to 10^{-10} Torr.

3.2. Auger Electron Spectroscopy

3.2.1. Introduction

Auger Electron Spectroscopy (AES) is the surface technique most commonly employed to determine the elemental composition of a surface. Because it determines the composition of only the top few layers of a surface, it is suitable as a means for identifying surface impurities. It can detect less than 5% of a monolayer of many impurity species. Lander first suggested the use of AES for detection of surface impurities (Lander, 1953). In 1968 Harris demonstrated that

energy analysis of Auger electrons excited by electron bombardment is a powerful technique for chemical analysis of solid surfaces (Harris, 1968). Since then, this analytical technique is been used in numerous materials applications, especially those requiring surface specificity and high spatial resolution.

3.2.2. Principles

The history of AES goes back to 1925, when the French physicist Pierre Auger first described the *Auger process* (Hedberg, 1995). Auger spectroscopy presupposes three basic steps:

(1) Atomic ionization (by removal of a core electron);

(2) Electron emission (the Auger process);

(3) Analysis of the emitted Auger electrons.

Following core level ionization, an atom will relax to a lower energy state through a two electron coulombic rearrangement that leaves the atom in a doubly ionized state. The energy difference between these two states is carried away by the emitted Auger electron which has a kinetic energy specific of the parent ion (Hedberg, 1995), and the atomic levels involved.

In the following discussion, the Auger process illustrated (using X-ray spectroscopy nomenclature) is KL_1L_{23} (corresponding to 1s, 2s & $2p_{1/2;\ 3/2}$ states in optical spectroscopy nomenclature).

The Auger process starts by creation of a core hole - this is typically accomplished by bombarding the sample with a beam of high-energy electrons

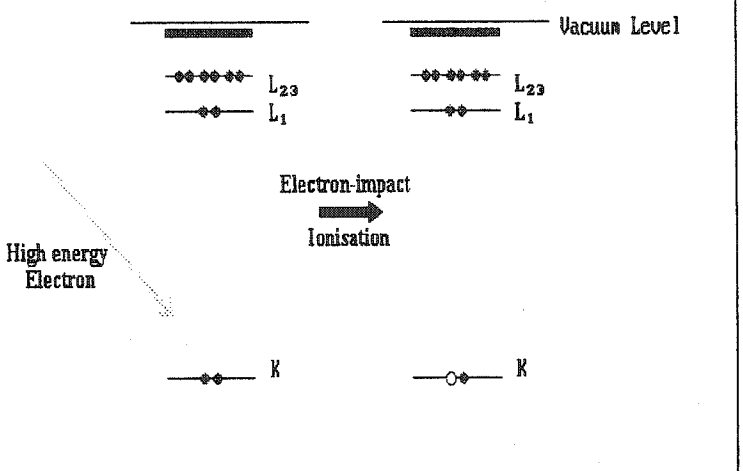

Figure 3.3. Atomic Ionisation
(http://www.chem.qmw.ac.uk/surfaces/scc/scat5_2.htm)

(2 - 10 keV).

In the diagram above (fig. 3.3), ionization is shown to occur by removal of a K-shell electron.

Relaxation and Auger Emission

The ionized atom that remains after the removal of the core hole electron is in a highly excited state and will rapidly relax back to a lower energy state by one of

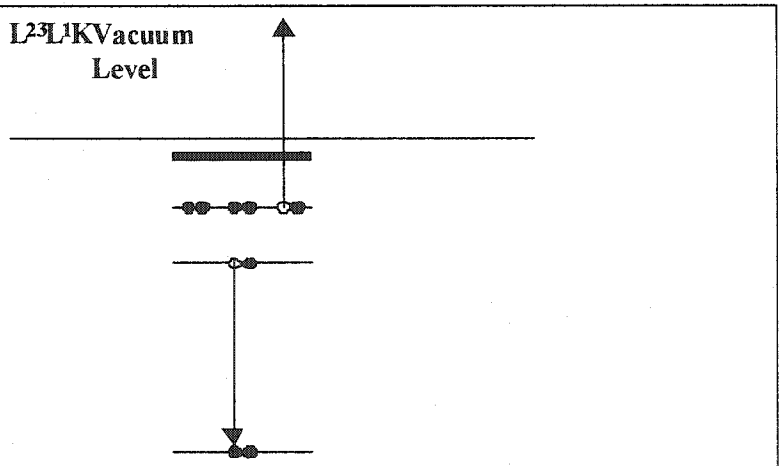

Figure 3.4. Relaxation and Auger Emission

(adapted from
http://www.chem.qmw.ac.uk/surfaces/scc/scat5_2.htm)

two mechanisms: X-ray fluorescence, or Auger emission.

We are not interested in the former mechanism and will only consider the latter one (schematically illustrated in fig. 3.4). In this example, one electron falls from a higher level to fill an initial core hole in the K-shell and the energy released in this process is simultaneously transferred to a second electron. A fraction of this energy is required to overcome the binding energy, and the remainder is retained by this emitted *Auger electron* as kinetic energy. In the Auger process illustrated above, the final state is a doubly ionized atom with core holes in the L_1 and L_{23} shells. The Auger electron kinetic energy roughly equals the difference in the binding energies of the K, L_1 and L_{23} energy levels:

$$KE \cong E_K - E_{L1} - E_{L23} . \qquad (3.2)$$

A more accurate description of the kinetic energy should take into account the hole-hole interaction, *U* (Woodruff and Delchar, 1994):

$$KE = E_K - E_{L1} - E_{L2,3} - U . \qquad (3.3)$$

The kinetic energy of the Auger electron is characteristic of the element that emitted it, and can thus be used to identify the element.

Electrons emitted in an Auger process do not travel very far through a crystal lattice before being recaptured (i.e., inelastic mean free paths of few atomic layers). This means that emitted electrons originate very close to the surface - in fact, we only see those created in the first few atomic layers. Thus the surface sensitivity of AES is ensured.

An Auger spectrum may plot the number of electrons detected versus electron kinetic energy, however it is more common to plot the first derivative spectrum (fig. 3.5).

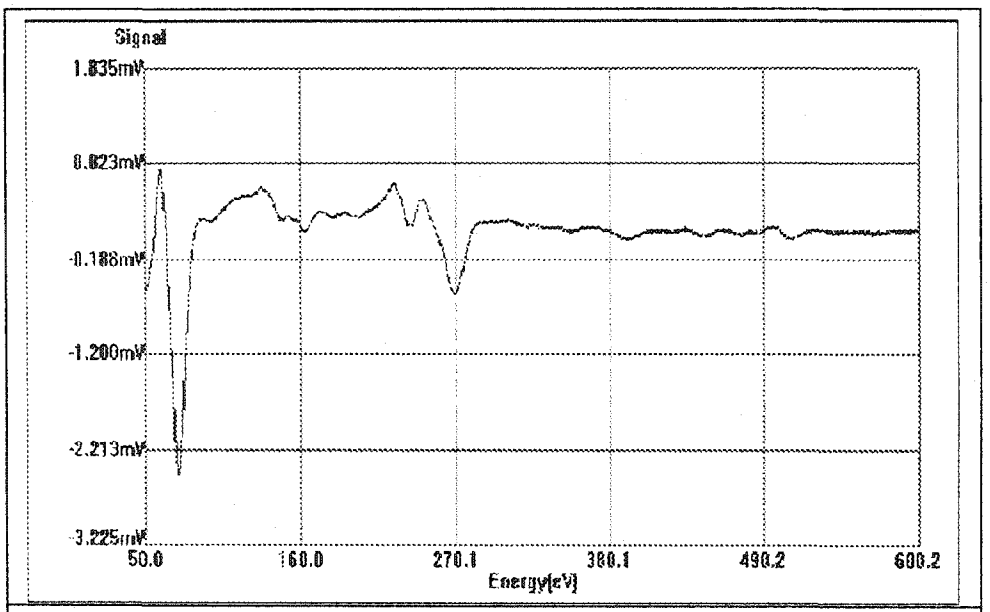

Figure 3.5. Auger Spectrum of a typical Au(111) surface. The main gold peak is situated at 74 eV. The other major peaks are C at 270 eV and O at 510 eV. There are also several smaller peaks, due to other gold transitions.

Elements are identified by the energy position of the Auger peaks (the energy of the largest negative excursion in the differentiated spectrum), while the intensity of the peak yields the concentration of the element. The observed Auger spectrum is compared with standard Auger spectra for the elements. The Handbook of Auger Electron Spectroscopy (Hedberg, 1995) comprises a first derivative survey of spectra for 81 elements displayed from 0 to 3200 eV. Direct spectra and first derivative spectra of specific energy regions are also included. Fig. 3.5 shows explicitly how to interpret an Auger Spectrum of Au(111).

Auger electron spectroscopy is able to detect virtually all elements, with the exception of hydrogen and helium (these two elements do not emit Auger electrons, since at least three electrons are required). Auger analysis is most often performed in UHV to avoid contamination of the surface during measurement from residual gas adsorption. Good vacuum also ensures the unobstructed passage of Auger electrons from the surface under study to the detector. The desired base pressure for an accurate Auger analysis is in the 10^{-10} Torr range.

3.2.3. Instrumentation

The Auger electron spectrometer employed in our lab is the Omicron Vacuumphysik GmbH (Taunusstein, Germany) Cylindrical Mirror Analyzer (CMA) 100 (fig 3.6). It consists of an electron gun to create the incident electron probe for specimen excitation, and an electron energy analyzer and detector for the measurement and collection of emitted electrons.

The electron source (a tungsten hairpin filament) fires a 3 keV beam of electrons at the probe's surface. The resulting Auger electrons are collected by the CMA and a channel electron multiplier (CEM).

The CMA is comprised of two concentric metal cylinders and CEM. A bias applied between the two cylinders gives the energy dispersive field of the CMA (fig. 3.7). The incident beam of electrons is focused to a point on the sample

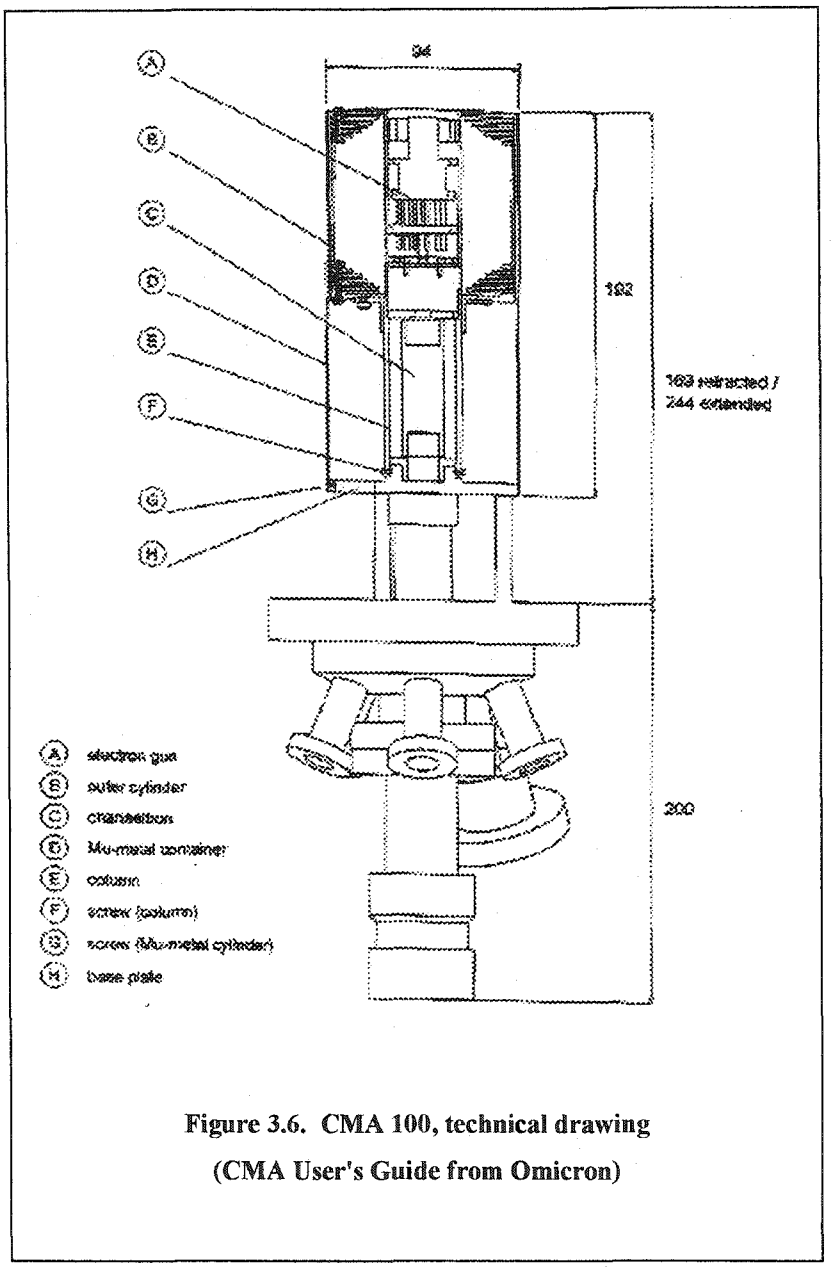

Figure 3.6. CMA 100, technical drawing
(CMA User's Guide from Omicron)

surface. Auger electrons move outward from this point in all directions. Some pass through the grid covered aperture in the inner cylinder. A variable negative potential on the outer cylinder bends the Auger electrons back through a second aperture on the inner cylinder and then through an exit aperture on the analyzer

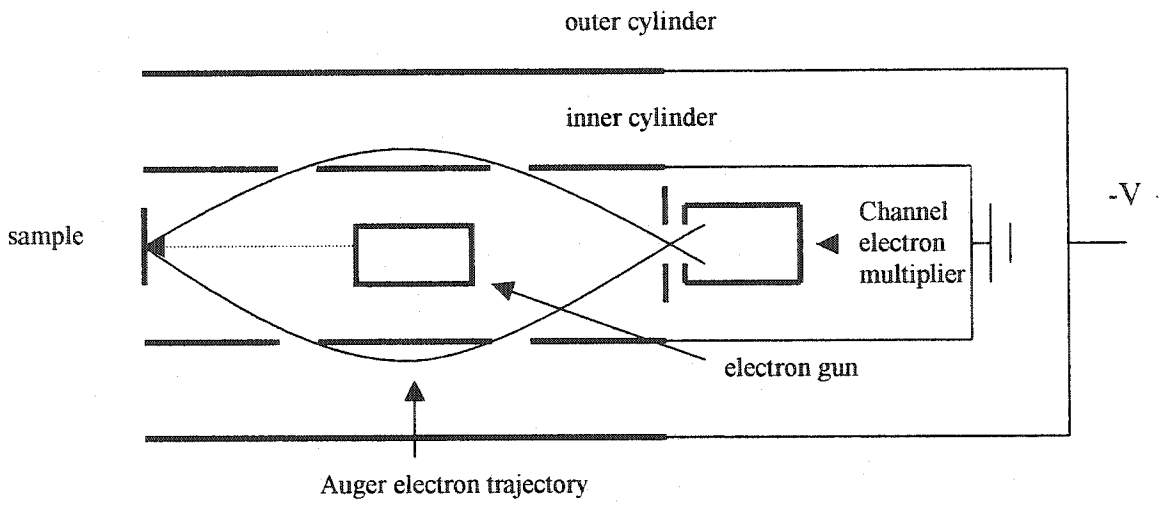

Figure 3.7. Schematic of a cross section of a cylindrical mirror analyzer
(adapted from http://www.eaglabs.com/cai/auginst/eeanal.htm)

axis. The energy of the transmitted electrons is proportional to the voltage (-V) on the outer cylinder. The electrons with the desired energy are then guided towards the CEM.

The channel electron multiplier (fig. 3.8) is basically an electron detector. The physical process that allows an electron multiplier to operate is called *secondary electron emission.* When an electron strikes a surface, it can cause the release of electrons associated with the outer layer of atoms. The CEM is shaped like a cornucopia and inside it is coated with a material that has a high secondary electron emission coefficient. Electrons are accelerated inside the CEM by the local electric field developed by the high bias voltage applied between the ends of the CEM. The accelerated electrons will trigger more secondary electron emissions when they hit the CEM surface. This electron cascading process

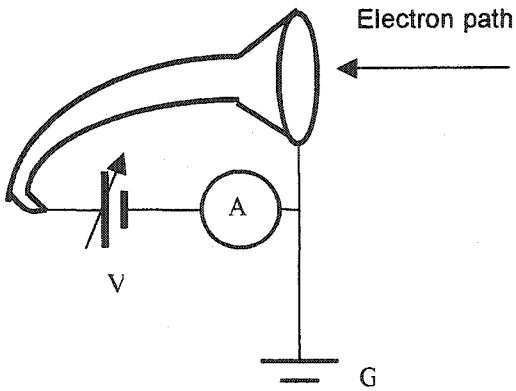

Figure 3.8. Channel electron multiplier.

A-signal meter; V-gain voltage; G-ground

(adapted from http://matsci.uah.edu/courseware/mts723/lectures/04topic/04d/04ddetectorsSC.pdf)

results in gains up to 10^7 (O'Hanlon, 1989). With the CEM, the number of electrons for a given energy is recorded.

In order to improve the signal-to-noise ratio, and also peak identification, the first derivative of the signal is measured using a lock-in amplifier. To get dN/dE, the single constant voltage source is replaced with a combination of a constant voltage source V_0 and a small sinusoidal voltage $\Delta V\cos\omega t$. The net effect of applying a modulating voltage $V=V_0+V\cos\omega t$ is to differentiate the signal with respect to energy. The signal current, $N(E)$,can be expanded as a Taylor series around V_0:

$$N(eV) = N(eV_0) + \left(\frac{dN}{dE}\right)_{eV_0} \Delta(eV)\cos\omega t + \ldots$$

Using the lock-in amplifier to detect the component of the signal with frequency ω yields a signal that is proportional to the first derivative dN(E)/dE.

3.3. Scanning Tunneling Microscopy

3.3.1. Introduction

The invention of the Scanning Tunneling Microscope (STM) by Gerd Binnig and Heinrich Rohrer at the IBM laboratory in Zurich, Switzerland came as a breakthrough in 1982. The instrument is capable of generating real space images of surfaces with atomic resolution. Five years later, the Nobel Prize was awarded to e two Swiss physicists, as an international confirmation of the importance of their invention.

Basically, the STM maps the surface topography by measuring the tunneling current between an atomically sharp tip and a conducting sample. It is an application of the concept of electronic tunneling. The apparatus developed by Binnig and Rohrer consisted of a large cylindrical metal frame that suspended

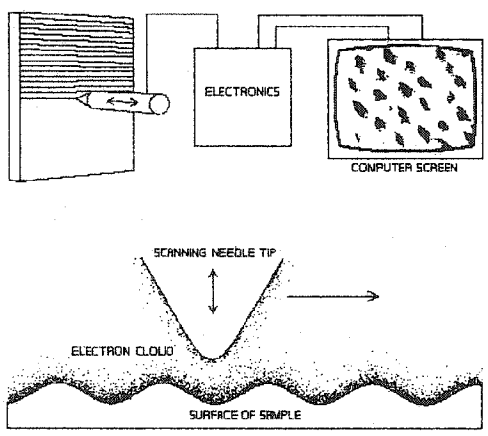

Figure 3.9. Schematic of the STM invented by Binning and Rohrer that was published in the August 1985 edition of *Scientific American* (http://www.mobot.org/jwcross/spm/)

the microscope mechanism and used springs and magnets for damping vibrations. Everything was inserted in a vacuum chamber and a fine tip was brought close to the surface of a solid using piezoelectrics (fig. 3.9). Applying a voltage between the tip and surface, the two researchers observed a tunneling current through this controlled vacuum gap and obtained atomic resolution images of the Si(111) 7×7 reconstruction (Binnig et al., 1982).

The STM has proven to be a very powerful tool for studies of solid conducting surfaces, down to atomic resolution. Nowadays, the STM is used worldwide in many disciplines in condensed matter physics, chemistry and biology. It is not restricted to vacuum, it can be used under ambient conditions, in an inert gas, in a liquid, and at temperatures ranging from mK to 1000 K (Bonnel, 1993).

3.3.2. Theory

The basic principle of a scanning probe microscope is to raster scan a probe with small lateral dimensions and distance-dependent interaction over the surface. The physical interaction used in obtaining the surface information for a scanning tunneling microscope is quantum mechanical tunneling.

Vacuum tunneling

Classical mechanics cannot explain how an electron passes from one metal across a potential barrier to another. This concept can only be explained using the dual (wave/particle) behaviour of an electron, introduced by quantum mechanics.

Let us consider two metals, one of which is the tip and the other is the surface, separated by a finite distance. This distance is represented by a uniform potential barrier, $U(x)$. The time-independent one-dimensional Schrödinger equation describing the wave properties of an electron in the tip is:

$$-\frac{\hbar^2}{2m}\frac{d^2\psi(x)}{dx^2}+U(x)\psi(x)=E\psi(x) \tag{3.4}$$

where E is the energy of the state, m is the electron mass, $\hbar = h/2\pi$, h is Planck's constant and U is the potential in the barrier.

The wave function of an electron in the tip can be described by the equation:

$$\psi(x)=Ae^{-ikx}+Be^{ikx} \tag{3.5}$$

where

$$k^2=2m(U-E)/\hbar^2 \tag{3.6}$$

For an electron in the substrate, the wave function has the same form, but with different coefficients. The wave function does not go to zero at the boundary of the metal, meaning that the probability that one electron will penetrate the potential barrier is non-zero.

If the gap between the two metals is on the order of 10 Å, an electron from one metal may tunnel to the other side of the barrier. The transmission probability, or the tunneling current, decays exponentially with barrier width s (Bonnell, 1993)

$$I \propto e^{-2ks} \tag{3.7}$$

Tunneling Hamiltonian Approach

For tip-sample distances on the order of 10 Å, the coupling of electronic wavefunctions across the barrier is weak and tunneling can be explained with first-order perturbation theory. The tunneling current described by first-order perturbation theory is

$$I = \frac{2\pi e}{\hbar} \sum_{\mu,\nu} \left\{ f(E_\mu)\left[1 - f(E_\nu)\right] - f(E_\nu)\left[1 - f(E_\mu)\right] \right\} \left| M_{\mu\nu} \right|^2 \delta\left(E_\nu + eV - E_\mu\right) \tag{3.8}$$

where *f(E)* is the Fermi function, *V* is the applied voltage, $M_{\mu\nu}$ is the tunneling matrix element between tip states ψ_μ and sample ψ_ν, E_μ is the energy of ψ_μ and E_ν corresponds to ψ_ν(Stroscio and Kaiser, 1993). The Greek letters μ and ν refer to the tip and sample, respectively.

In the case of small voltages, equation (3.8) is reduced to

$$I = \frac{2\pi}{\hbar} e^2 V \sum_{\mu,\nu} \left| M_{\mu\nu} \right|^2 \delta(E_\nu - E_F)\delta(E_\mu - E_F) \tag{3.9}$$

The main problem is the calculation of the tunneling matrix element. Bardeen (1960) evaluated it as

$$M_{\mu\nu} = -\frac{\hbar^2}{2m} \int dS \cdot (\psi_\mu{}^* \nabla \psi_\nu - \psi_\nu \nabla \psi_\mu{}^*) \tag{3.10}$$

where *dS* is an element of surface within the barrier region, *m* denotes the electron mass, and the term inside the brackets is the current density $j_{\mu\nu}$ operator. Because the tip wave functions necessary for the calculation are not

known, approximations must be made. For a spherical tip they assume wave functions of pure *s*-character (quantum number *l*=0). At low temperature and for small tunneling voltages (Tersoff and Hamann, 1983, 1985), the following simplified expression for the tunneling current is obtained

$$I \propto \sum_{\nu} |\Psi_{\nu}(r_0)|^2 \delta(E_{\nu} - E_F) \equiv \rho(r_0, E_F) \tag{3.11}$$

In this equation, $\psi_{\nu}(r_0)$ is the wave function of the sample at the position of the centre of curvature of the tip, E_F is the Fermi level at the sample surface, and the quantity $\rho(r_0, E_F)$ is the local density of states of the sample. Equation (3.11) shows that the tunnel current is directly proportional to the local density of electronic states of the sample near the Fermi level at the position of the tip. Because the wave functions decay exponentially in the *z*-direction perpendicular to the surface, one can write

$$\Psi_{\nu}(r) \propto \exp(-\kappa z) \tag{3.12}$$

and, implicitly,

$$|\Psi_{\nu}(r_0)|^2 \propto \exp(-2\kappa(s+R)) , \tag{3.13}$$

where *s* is the distance between the sample and the front most tip orbital. Thus, as expected, the tunneling current depends exponentially on the distance *s*

$$I \propto \exp(-2\kappa s) . \tag{3.14}$$

Hence the tunnel current decays exponentially with the barrier width *s*.

3.3.3. Operating principles

The scanning tunneling microscope is essentially a very sensitive profilometer that uses quantum mechanical tunneling as the sensing method. A small metallic probe is scanned across a sample surface by piezoelectric transducers (figure 3.10). These transducers provide motion in three orthogonal directions. A sawtooth waveform rasters the probe in the x-direction, while a ramp voltage advances the raster signal in the y-direction. With this notation, the probe-sample distance is on the z-axis. A third voltage adjusts this z distance so that the probe and sample remain separated by a few angstroms creating a small vacuum potential barrier. Scanning a metal probe a few angstroms from a surface is

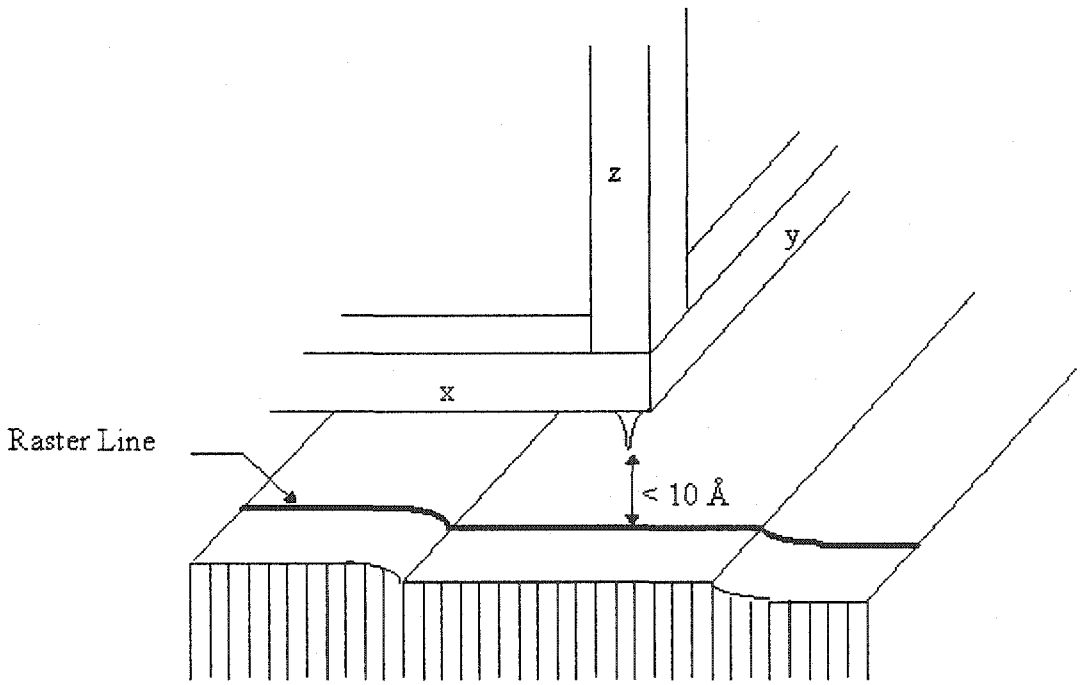

Figure 3.10. Schematic diagram of STM
(http://www.phys.ttu.edu/~tlmde.html)

usually impossible without some type of feedback and control system. A tunneling current across the vacuum barrier provides the input for such a feedback and control system. Due to the overlapping the electron wave functions in the metallic probe and the sample, a tunneling current flows when a bias is applied between the probe and sample. Amplifying this tunneling current and comparing it to a set point value creates a signal suitable for feedback to the voltage applied to the z piezoelectric transducer. This feedback loop created by the tunneling current and the z piezoelectric transducer voltage maintains a constant separation distance between the probe and sample as scanning occurs, creating an array of z voltages that represent a contour plot of the sample.

Piezoelectric transducers are central to the operation of the STM. These transducers provide the finely controlled motion for the demands of the STM operation. Piezoelectric materials are ceramics with the distinct property of changing dimensions in response to an applied voltage, and vice-versa. As a consequence, piezoelectric scanners can be made to move in all three dimensions, expanding in some directions while contracting in others. The material usually employed is lead zirconium titanate (PZT), with various dopants added in order to create specific material properties.

Scanning tunneling microscopes can function in two modes: constant height and constant current modes. However, the latter mode is most commonly used. In constant-current mode, STM uses feedback to keep the tunneling current constant by adjusting the height of the scanner at each measurement point.

When an increase in the tunneling current is detected, the system adjusts the voltage applied to the piezoelectric scanner to increase the distance between the tip and the sample. In this case, the motion of the scanner constitutes the data set. If the system keeps the tunneling current constant within a few percentage points, the tip-to-sample distance will be constant to within a few hundredths of an angstrom.

3.3.4. Instrumentation

The homemade STM employed in the lab (shown in fig. 3.11) belongs to the Besocke "beetle" type (Besocke, 1987), with a control system developed by RHK Technology (Rochester Hills, USA). It consists of three supporting piezo tubes

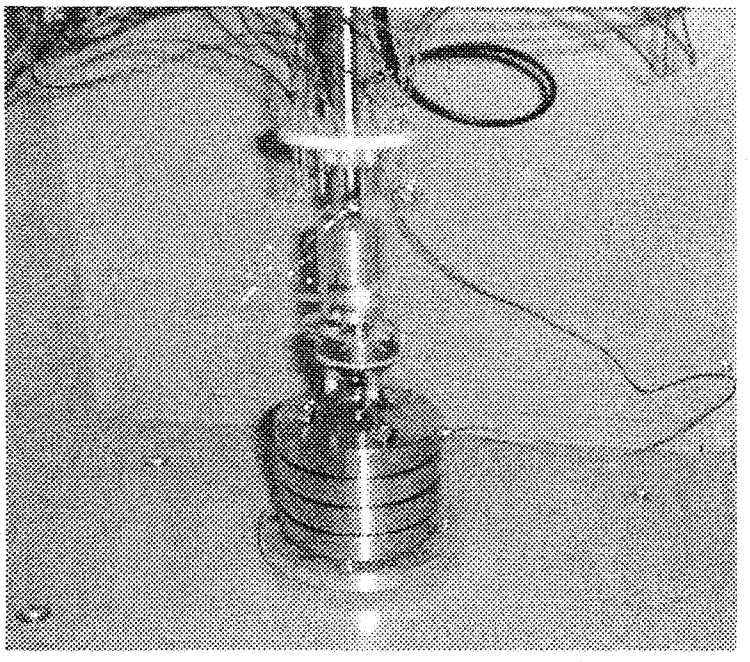

Figure 3.11. The STM in use in our lab

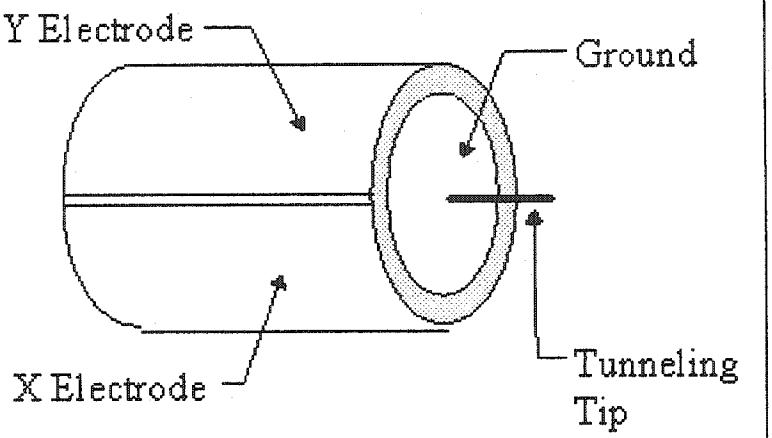

Figure 3.12. Piezoelectric tube scanner
(http://www.phys.ttu.edu/~tlmde/thesis/DESIGN_AND_CONSTRUCTION.html)

arranged in a triangle configuration and terminated with sapphire balls, and a central scanning piezo tube, which is laid-out as a *single tube scanner* (fig. 3.12). All four piezoelements are bonded tightly to a stainless steel base. The tunneling probe is a fine wire made of a platinum-rhodium alloy and is mounted in the centre of the free end of the tube scanner (fig. 3.13).

Applying a voltage to all four quadrants that constitute the scan tube, while grounding the inner electrode, causes a change in the length of the tube, thus providing the motion of the tip in z direction. If a voltage is applied to one of the quadrants while the other quadrants are grounded, the length of the corresponding quadrant changes, creating a horizontal deflection in the end of the tube. Thus, bending the tube produces the scanning motion (x and y).

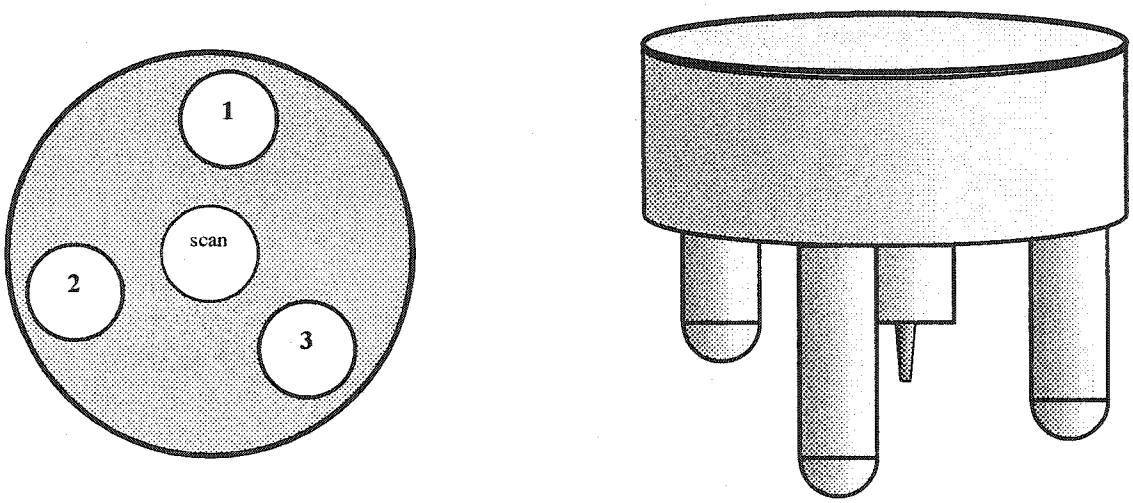

Figure 3.13. A Besocke-type STM scan head is comprised of a solid disk supported by three piezo legs, and a central single tube scanner; view from below (left) and lateral (right).

Measurements are done by positioning the STM head on a circular three-step brass ramp surrounding the sample. The coarse approach of the tip is accomplished by applying a variable DC voltage to the z-electrodes of the piezo legs. First the scan head is lowered mechanically with a lever construction onto the circular ramp. Coarse sample positioning presents a challenging design problem in the STM, as it must provide a fine enough motion so that the tip approaches to within nanometers of the surface without crashing into the sample. For coarse approach, a "stick-slip" method was used. A sawtooth voltage waveform is applied to the three outer legs. As the voltage ramps up, the piezo legs bend tangent to the ramp. At the peak of the waveform an abrupt voltage drop makes the legs rapidly straighten. The result of this alternating motion is the scan head rotates down the ramp to find a tunneling current. The three piezo

legs also allow for coarse positioning in X and Y, allowing large areas of the sample to be imaged.

All images shown in this thesis are recorded in the constant current mode, where the distance between the tip and the sample is adjusted during scanning in order to keep the tunneling current constant.

4. SAMPLE PREPARATION

4.1. Gold evaporation

The materials employed in this study were 99.99% pure gold purchased from Marivac Canada Inc. (St. Laurent, Quebec) and green muscovite mica available from Structure Probe, Inc. (West Chester, Pennsylvania). The mica was cut into 1×1 cm pieces and then cleaved in air using adhesive tape. Subsequently, the mica substrates were fastened by molybdenum strips to a stainless steel or tantalum sample holder (see fig. 4.1) and immediately loaded via an airlock into the multi-chamber vacuum system. The load-lock permitted rapid sample loading, and sequential deposition and storage of samples without breaking the main vacuum. The vacuum system was previously pumped down and then baked to eliminate any moisture so that the base pressure reached 10^{-10} Torr. The mica substrates were handled with gloves and clean tools to avoid any fingerprint contamination.

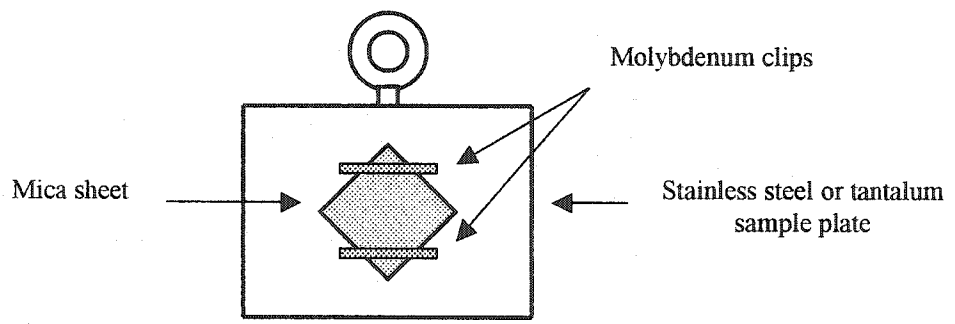

Figure 4.1. Schematic of sample holder

While cleavage of mica in air reveals an atomically flat surface, a further requirement for a suitable gold deposition substrate is that this surface be absolutely clean. A Freshly cleaved surface of mica is quickly covered with physisorbed and chemisorbed water (Dishner et al., 1998) which can inhibit gold adhesion. Therefore, in order to promote gold adhesion, the mica substrates were annealed in the main UHV system, prior to gold deposition, at a temperature of 340°C, for periods of time varying from 6 to 52 hours. For annealing the samples were positioned on a stainless steel stage on the main manipulator and heated radiatively from the back through the sample holder. The temperature of the mica during annealing was monitored by a K-type thermocouple placed on one of the radiation shields between the filament and the sample stage (sample stage-filament distance is 2-3 mm). Samples were allowed to cool to room temperature (~30°C) in the main chamber before being transferred, under vacuum, to the evaporation chamber for gold deposition.

Gold was evaporated in a chamber with a 10^{-8} Torr base pressure using a resistively heated tungsten-wire conical basket. The vacuum in the evaporation chamber was achieved via a turbomolecular pump backed up by a mechanical pump, and chamber was connected to the main UHV chamber via a gate valve. The 1 or 0.1 mm gold wire was first melted in the tungsten basket. Before evaporation, the basket was heated up in order to outgas contaminants. Deposition rates ranging from 0.2 to 3 Å/s were determined by a XTM/2 Leybold Inficon (Syracuse, New York) quartz-crystal microbalance (QCM). The microbalance utilizes the piezoelectric qualities of quartz crystals. The crystal is

very sensitive to mass changes associated with the deposition of material onto the surface. The mass change produces a change in the resonant frequency of the QCM. All gold evaporations were intended to produce films of identical thickness. This was accomplished by varying both the rate and duration of

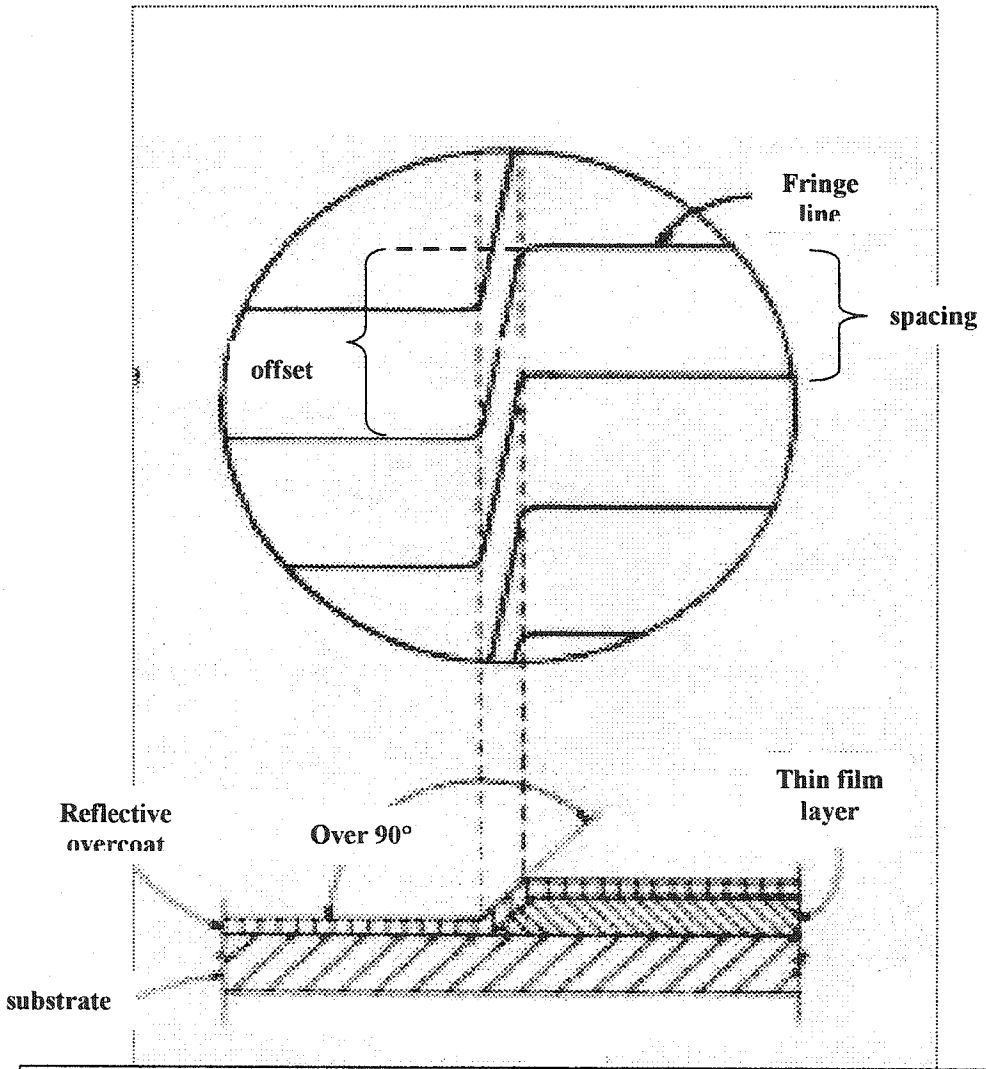

Figure 4.2. Illustration of the principle of measurement of film thickness, using the Fizeau interferometer (Varian, 1966)

deposition accordingly. Film thickness was measured using the QCM calibrated against a Varian's (Lexington, MA) Fizeau interferometer. This instrument

employs a sodium vapor lamp and optics to direct light through a Fizeau plate which makes contact with the sample at a slight angle and forms an air wedge between them. An interference fringe pattern is produced in the air wedge and is viewed through a filar eyepiece on the interferometer. The spacing (distance between fringe lines) and shape of the fringe lines can be interpreted to determine an accurate contour map of the sample surface. A displacement of a fringe line occurs when it encounters a vertical variation, such as the edge of a thin film layer, on the surface of the sample (fig. 4.2). The film thickness is determined by measuring the fringe offset in relation to the 2946 Å (one-half of the wavelength of the sodium vapor light source) spacing of the fringe lines, as shown in the formula:

$$\textit{Film thickness}\ (\text{Å}) = [(\textit{fringe offset}) / (\textit{fringe spacing})] * 2946\ \text{Å}$$

For this experiment, a glass substrate was used instead of mica, since mica had steps on it due to different layers exposed and tended to deform when put in the interferometer. The glass was harder and did not have these abrupt steps.

Preparation of the glass slide consisted of thoroughly washing it with soapy

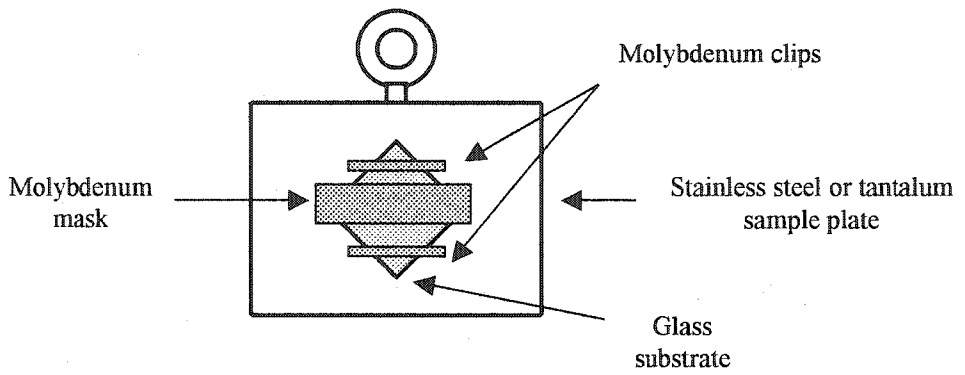

Figure 4.3. Schematic of substrate set-up for thickness measurement using a Fizeau interferometer

water, and alcohol. It was then subjected to the flame of a Bunsen burner. A molybdenum strip was then spot-welded to cover part of the glass, as shown in fig. 4.3. The glass was immediately loaded into the evaporator. A gold film of the usual thickness (yet to be determined) was deposited. After deposition, the molybdenum strip was removed and a second Au film was deposited. The second film covers the entire surface of the substrate including the region covered by the molybdenum mask in the first evaporation. There is a different film thickness in the region that was covered by the mask, and the region that received two coatings. This difference can be measured directly by the interferometer. Typical film thickness, as determined using the above procedure, was ~640 Å.

The substrates were not heated intentionally during evaporation, and since the distance between the W-basket and the sample plates was ~15 cm, radiative heating was negligible. Therefore, the temperature during evaporation was close to room temperature (~30°C). The pressure during evaporation varied between 10^{-7} and 10^{-8} Torr. After deposition, the samples were allowed to cool slowly to ambient temperature and were transferred to the main vacuum chamber for further study.

4.2. Probing the cleanliness of the sample

The cleanliness of samples was always tested using Auger electron spectroscopy. For this, the gold films were mounted onto the main manipulator

and the surface of interest was exposed for analysis. The observed Auger spectrum was compared to the standard Auger spectra for the elements, using the Handbook of Auger Electron Spectroscopy (Hedberg, 1995).

The Auger spectra for the vast majority of our samples exhibited three major peaks (fig. 4.4): the largest one is gold at 74 eV. A relatively small carbon peak shows at 270 eV, due to the fact that the W basket used for evaporation gives off CO when heated (in general, any part of the chamber that was in close proximity to the basket could get hot during evaporation and could potentially emit CO). The oxygen peak around 510 eV is also attributed to the existence of CO gas in the vacuum chamber.

4.3. Post-deposition thermal treatment

Subsequent to gold film deposition, the samples underwent one of two thermal steps: 1) post-deposition annealing, or 2) flash heating.

1) All annealing treatments were carried-out *in-situ* without breaking vacuum. We used the same heating stage in the main UHV chamber as used in pre-annealing. Post-deposition annealing of the gold films was conducted at the mica pre-deposition annealing temperature for various times and at temperatures of between 80 and 340°C (~1/3 of the melting temperature of gold 1064°C). After annealing, samples were left to cool slowly to ambient temperature.

Samples were analyzed with AES, before and after annealing. The comparison (fig. 4.4) revealed no modification in both position and size of gold peak.

However, during annealing the samples suffered further CO contamination. This was inevitable given the extended periods of exposure to background gases during annealing.

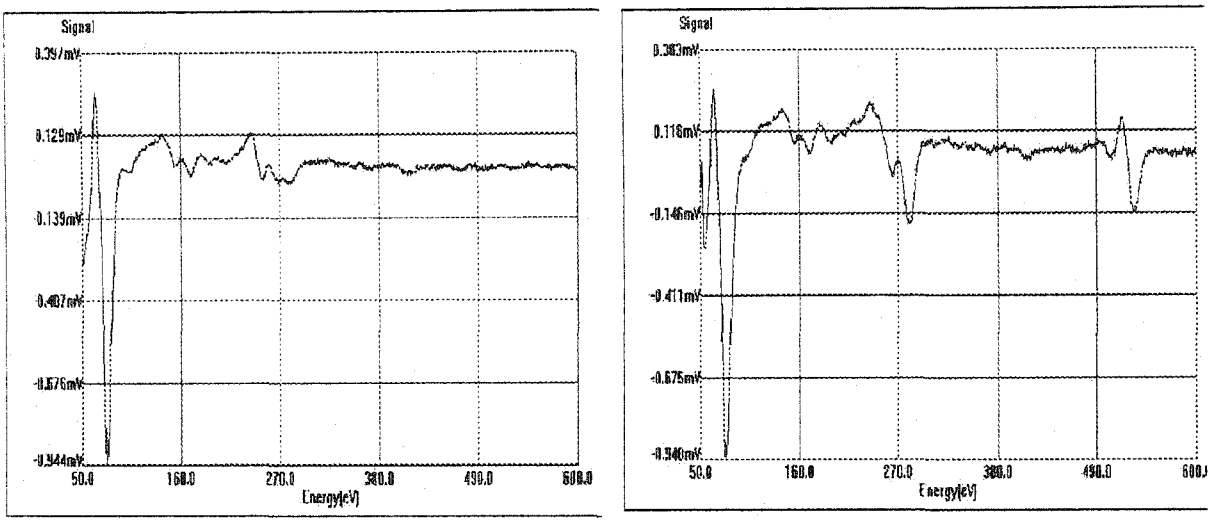

Figure 4.4. Auger spectra for gold film before (left) and after (right) annealing at 340 C for 3 h and 30 min. CO contamination appears during annealing.

2) *In-situ* flash annealing was possible by rapidly heating the films using the same heating stage. The filament was heated by 9 A of current. This ensured an extremely rapid (approximately 10 s) heating of samples. Several consecutive experiments during which the flashing temperature was varied were conducted. When the temperature hit the target value, all power sources were shut off and the samples were allowed to cool to room temperature. Flashing temperatures ranged from 650 to 300°C. Liquid nitrogen was used to protect the copper dewer of the main manipulator, and to ensure rapid cool down.

4.4. STM imaging

After cooling to room temperature, samples were removed from vacuum and STM measurements performed. All STM investigations were done at room temperature in air. Gold films were mounted on the STM sample holder and then placed in the centre of the three-segment circular ramp. Pt/Rh tips were freshly cleaved by mechanically cutting them at an angle using wire cutters. For each film, several 512×512 pixel images were taken in constant current (topographic) mode. Typically, two images (scan areas 0.5 μm×0.5 μm and 2000 Å×2000 Å) for three different regions of each film were obtained and analyzed. Bias voltages used for these experiments were typically around -1 V and the tunneling currents were kept at 1nA. All images presented in this thesis were altered for background subtraction using the image processing macros of the STM software (RHK Technology SPM 100).

5. RESULTS AND DISCUSSION

We studied the structure of the Au films prepared under a variety of preparation conditions. Initially the effect of mica pre-annealing time on the gold surface topography was investigated. The temperature of mica annealing was typically 340°C, while the duration of annealing ranged from 0 to 52 hours. The deposition in all cases was done at room temperature, the rate was kept constant (1.1 Å/s), and the pressure in the evaporator during deposition was in the range of 10^{-7} Torr. Figure 5.1 gives a qualitative illustration of the effect of mica annealing. All images are 0.5μm×0.5μm.

Evaporation of gold onto unannealed mica substrates at room temperature results in polycrystalline films that are comprised of a large number of very small crystalline grains (fig. 5.1a). Our scanning tunneling microscopy images disclose a pebble-type construction with an average grain size (AGS) of ~220 Å. The gold islands also exhibit rounded shapes. These results are consistent with results reported by Chidsey et al. (1988), Putnam et al. (1989), Watanabe et al (1991), and Dishner et al. (1998).

With increasing duration of mica baking, the grain size becomes larger (fig.5.1b), and some evidence of crystalline terraces appear. Atomic steps on top of these terraces can also be seen (fig. 5.1c and d). The gold grains seem to lose the spherical aspect, their contours being now composed of straight lines. Fig. 5.1d) shows hexagonal step edges characteristic of the (111) close-packed plane of fcc metals such as Au. This observation suggests that gold crystallites having (111) orientation have developed on mica. This is reasonable to expect, since the

(111) surface is the most stable for the fcc crystal structure (Watanabe et al., 1991).

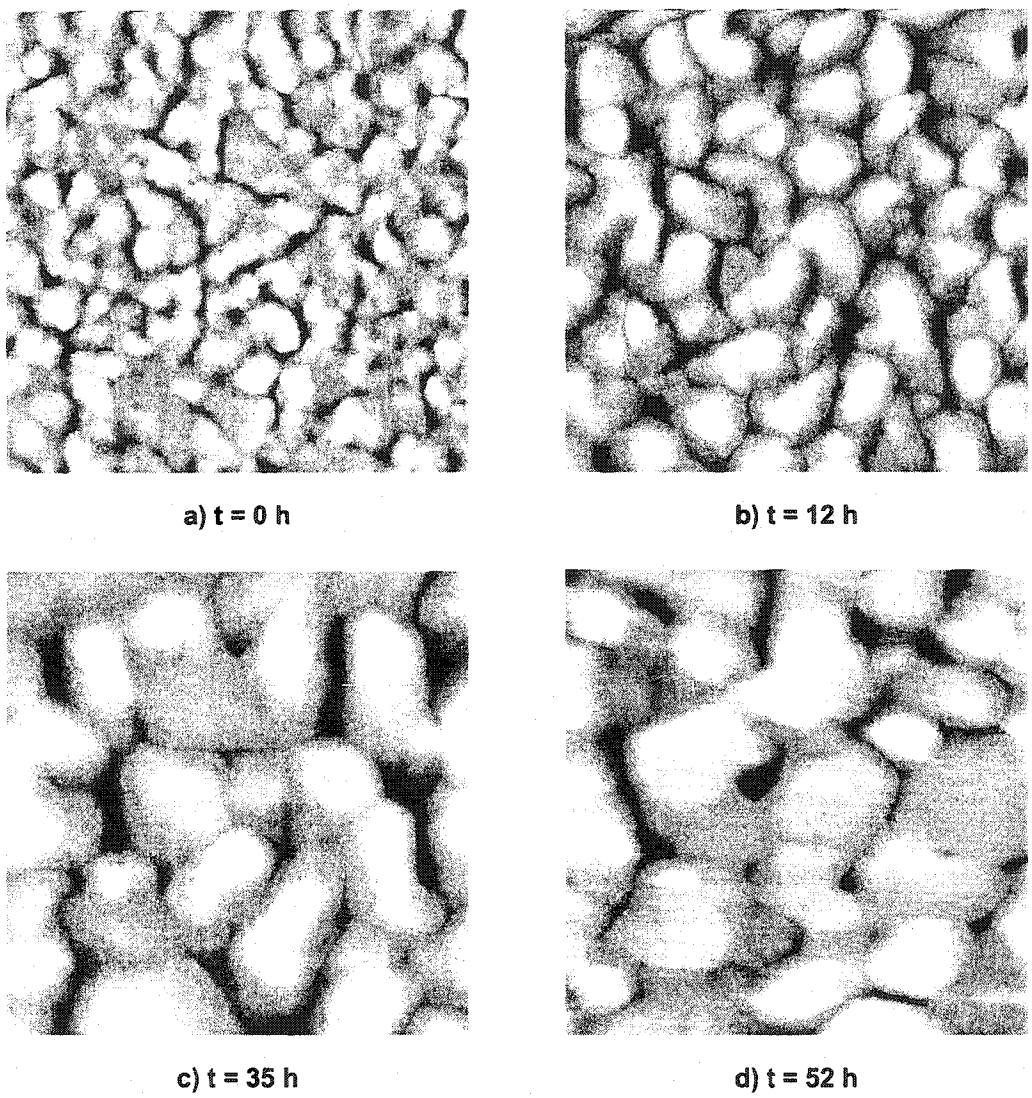

a) t = 0 h

b) t = 12 h

c) t = 35 h

d) t = 52 h

Figure 5.1. STM images (scan area: 0.5μm×0.5μm) of Au evaporated on room temperature mica, with mica annealed at 340°C for different periods of time.

Rms surface roughness values: a) 16.1 Å; b) 18.7 Å; c) 31 Å; d) 56.4 Å

Figure 5.2 is a plot of AGS versus mica baking time prior to deposition. The AGS values used for this plot were calculated by averaging the values obtained for grain size from several 0.5×0.5 μm^2 STM images at each mica baking time. The

temperature during baking was held at 340°C. The trend in the data points indicates that long bake-outs of the mica induced grain enlargement. The gold

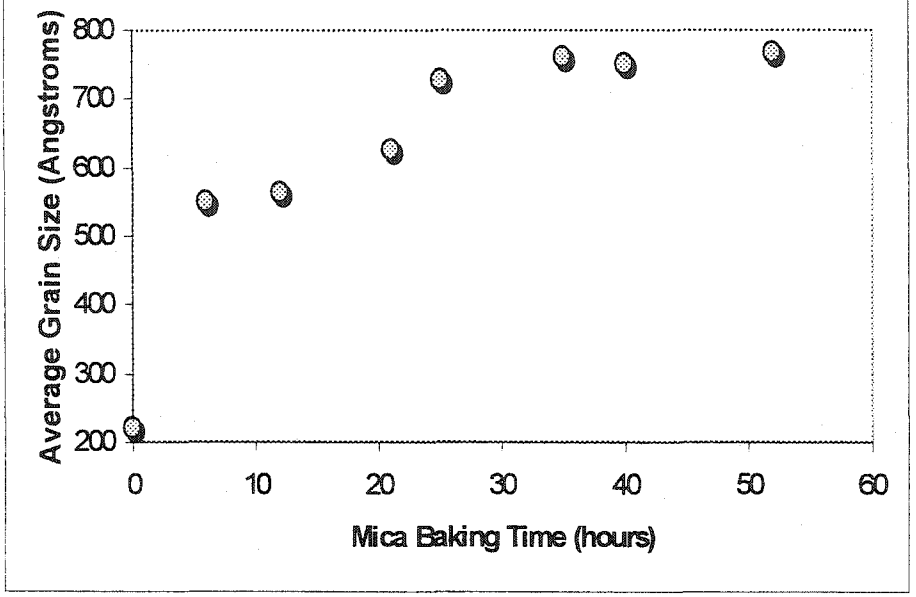

Figure 5.2. A plot of the average grain size versus mica baking time before evaporation of the gold.

grains were ~3.5 times larger when the mica was baked for 52 hours, compared to the case when mica was not baked at all. The rise was most abrupt for baking times between 0 and 24 hours. After 24 hours, it seemed that the grain size saturates. From the plot in figure 5.2, it is clear that there are at least two distinct processes that lead to an increase in the AGS. The dramatic increase at short baking times is due to removal of contamination on the mica surface (DeRose et al. (1991) reported that contamination on mica surface prevents direct adsorption of Au atoms onto it). Further increase of the grains size with prolonged mica baking may be attributed to either removal of water from inside the mica layers or

modification of mica structure, or both, we cannot make a definite statement at this time.

We also measured the surface roughness of each sample. A macro within the software gave us the rms surface roughness values (standard deviation of the *z* values), σ, for each image, using the following algorithm:

$$\sigma = \sqrt{\frac{1}{N-1}\left[\sum_i (z_i - \langle z \rangle)^2\right]}$$

where z_i is a height datum, <z> is the average of the height data, and *N* is the total number of data points per image (de Rose et al., 1991). Our experimental results indicate that film roughness increases with duration of mica annealing. A likely reason is that with prolonged mica baking larger grains are produced, both in the plane of the surface and normal to it.

*

In a second set of experiments we investigated the effect of the evaporation rate on film structure. The mica was pre-annealed for ~50 hours at 340°C, prior to evaporation, and the evaporation rate was varied between 0.2 Å/s and 3 Å/s.

Figure 5.3 gives a qualitative demonstration of the evolution of the average surface-grain size as a function of gold deposition rate. STM images reveal that the surface is comprised of textured gold islands. Small terraces with well-defined atomic steps are observed. The hexagonal shapes specific to the (111) close-packed plane are more evident on the surface of the film obtained by evaporation of gold at a rate of 0.2 Å/s (fig. 5.3a). A visual inspection of all images reveals that higher deposition rates induce a noticeable decrease in the

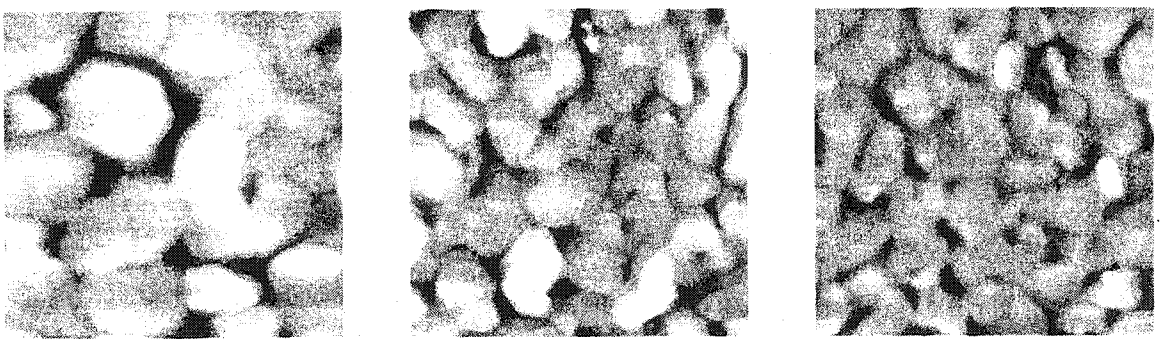

a) Φ = 0.2 Å/s b) Φ = 1.1 Å/s c) Φ = 2.2 Å/s

Figure 5.3. STM images (scan area: 0.5μm×0.5μm) of Au evaporated on room temperature mica, at various depositions rates.

Rms surface roughness values: a) 11.1 Å; b) 12.4 Å; c) 49.4 Å

average size of the gold grains (figs. 5.3b and 5.3c).

Figure 5.4 is a plot of the AGS versus gold deposition rate. As before, the AGS was obtained by averaging the values extracted from several 0.5×0.5 μm^2

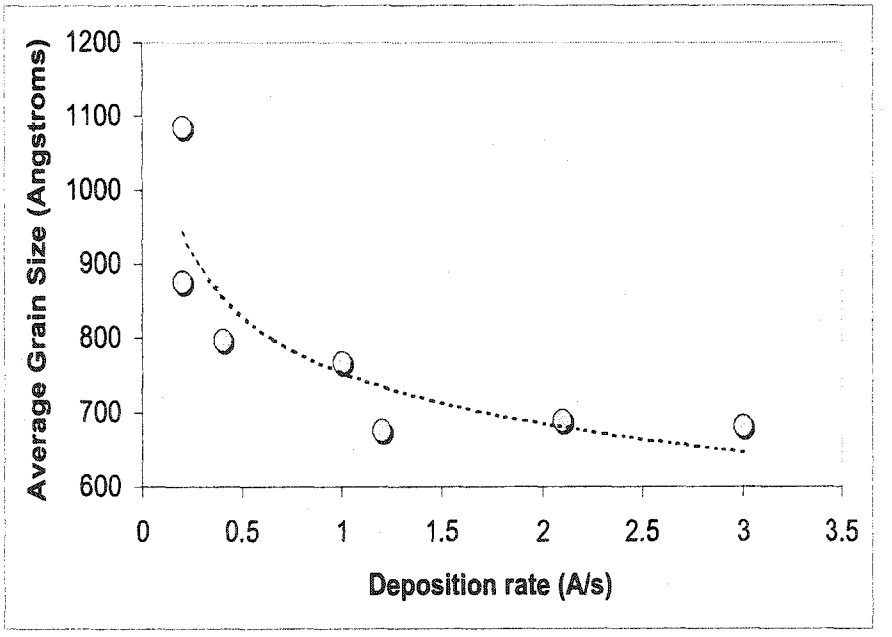

Figure 5.4. A plot of the average grain size versus deposition rate for the Au evaporation.

images at each particular deposition rate. The trend indicates that lower deposition rates produce larger gold grains. Grains are ~1.4 times greater for a deposition rate of 0.2 Å/s compared with a deposition rate of 3 Å/s. More specifically, the average dimension of the crystallites monotonically decreases from ~1000 Å, for a deposition rate Φ=0.2 Å/s, to ~680 Å at Φ=3Å/s. The plot in fig. 5.4 indicates that the decrease in the average grain dimension is sharp for low deposition rates (up to 1.1 Å/s). For Φ values greater than 1.1 Å/s, the grain size appears to be independent of the deposition rate.

Figure 5.5 displays the same data displayed on a log-log graph. Assuming a power law relationship between the AGS and the deposition rate, a line of best fit is obtained to extract an exponent.

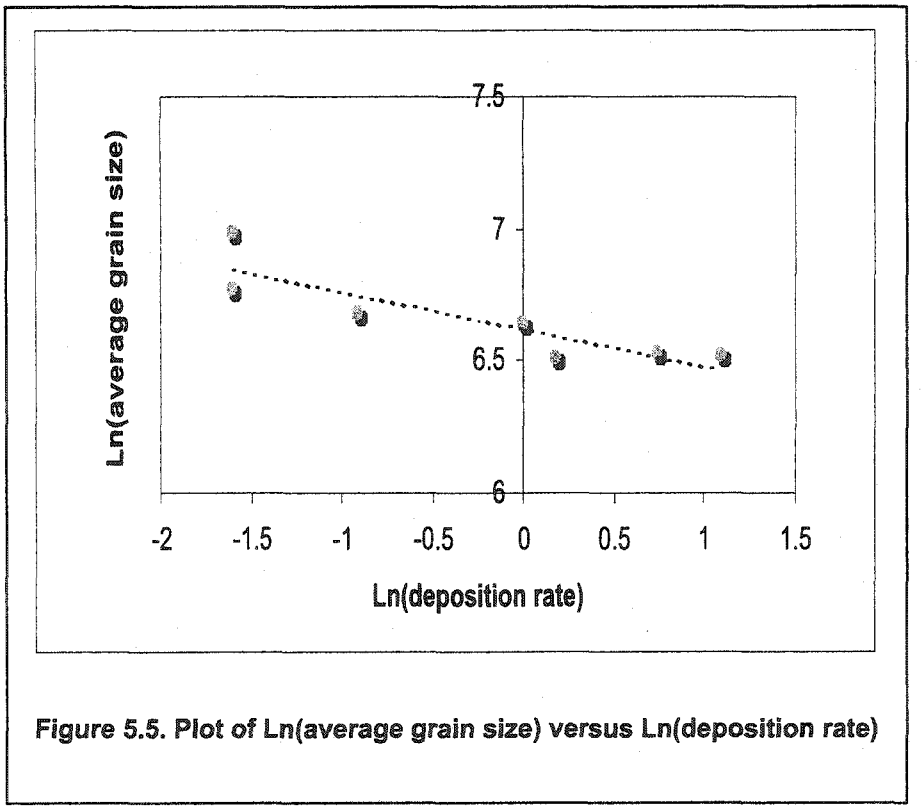

Figure 5.5. Plot of Ln(average grain size) versus Ln(deposition rate)

The data yields an exponent of ~0.30. This is in good agreement with the exponent predicted by kinetic Monte Carlo simulations of diffusion mediated island growth (Venables et al., 1984, Bartelt et al., 1992). These papers study island nucleation at submonolayer coverage (before coalescence) and predict a scaling law exponent of i/(i+2) where *i* is the critical nucleus. An exponent of 1/3 indicates a critical nucleus of one, or in other words, an island is nucleated whenever two adatoms meet on the surface. In gold data, this same exponent is observed well after coalescence. In summary, grain size is influenced by the rate of deposition, since higher deposition rates produce higher nucleation rates and thus a higher density of islands.

We also found that all samples display an increased rms roughness at higher deposition rates (fig. 5.3). Our result is not consistent with de Rose et al. (1991) who found that evaporation rate did not affect the smoothness of the substrate, as long as it was kept below 10 Å/s. Putnam et al. (1989) also recommend higher deposition rates for smoother films. However, both studies were done on gold deposited on heated mica substrates, and, moreover, the latter study investigated only deposition rates greater than 10 Å/s.

*

To summarize, we have found that with appropriate choice of mica anneal and deposition rate, gold evaporated on mica at room temperature, even without any subsequent thermal treatment, produced surfaces with relatively large flat terraces.

To further enlarge the grains, we investigated the effect of thermal annealing following growth. Generally, thermal annealing of metal films causes the grain boundaries to diffuse across the grains, and the grains merge. The films were prepared by evaporating the gold at a rate of 0.2 Å/s onto mica pre-annealed at 340°C for about 50 h. Two different post-deposition thermal steps were followed. In the first method the sample was held at temperature for a prolonged period, while in the second the temperature was ramped quickly to a target temperature at which point the heater was turned off.

Figure 5.6 offers a qualitative demonstration, using the first method, of the changes in the surface morphology as a function of post-annealing temperature. The upper limit on the annealing temperature was imposed by the highest temperature the mica could withstand, which was the same as the mica pre-annealing temperature (340° C).

Analyzing the sequence of 0.5 μm×0.5 μm STM images in fig. 5.6, one can see that annealing temperatures below 110°C have little effect on the size of gold crystallites. There is a visual similarity between fig 5.6a) (the film annealed at 110°C) and fig. 5.3a) (the as-grown film). Annealing at elevated temperatures produces increasing changes in the surface morphology. The film with the flattest and largest terraces (this is in principle the ideal character of a substrate for the study of deposited molecules) was obtained at an annealing temperature of 340°C (fig. 5.6d).

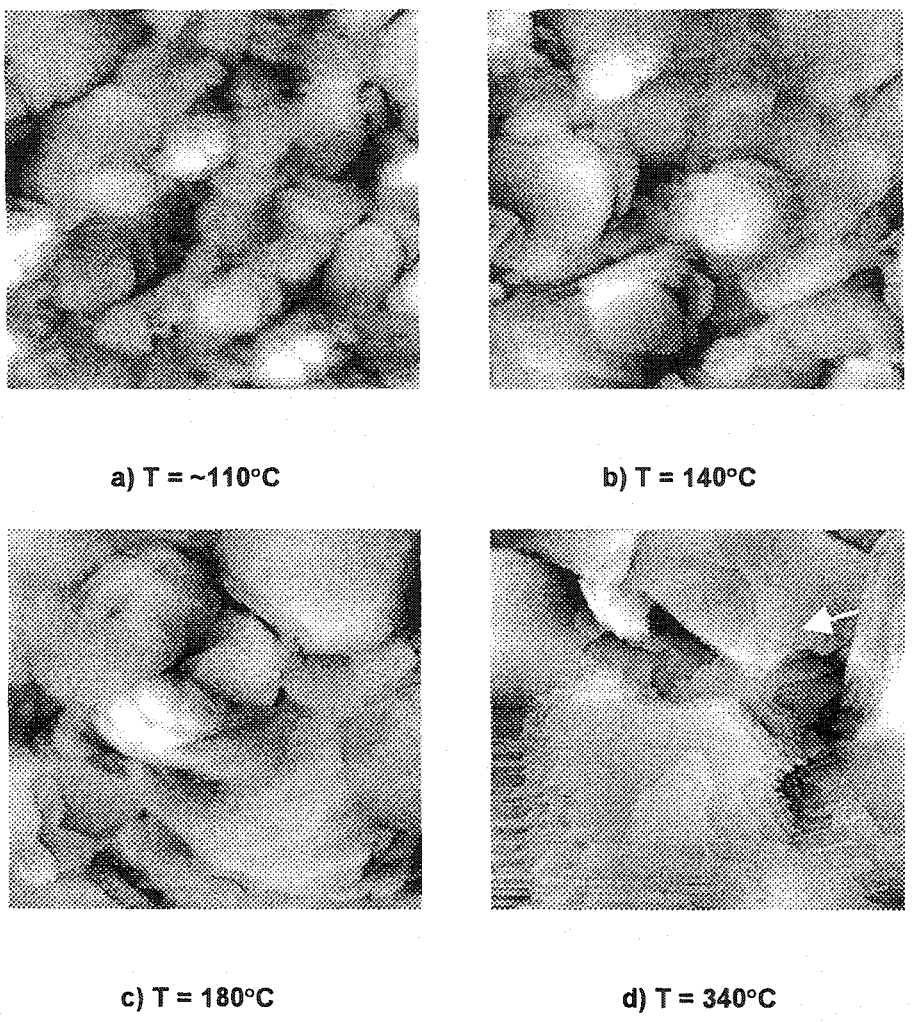

Figure 5.6. A series of 0.5 μm×0.5 μm STM images of gold films post-deposition annealed for 3 h and 30 min at different temperatures. The arrow in fig. d) points to a *screw dislocation*.

Rms surface roughness values: a) 6.76 Å; b) 4.59 Å; c) 5.7 Å; d) 18.8 Å

Figure 5.7 plots the dependence of the rms roughness on the annealing temperature. The data in the figure reveal no systematic change in roughness. All the data points are scattered between 4 and 8 Å- with the exception of one data point at 340°C. Due to the gap between 175 and 340°C, more data would be required in order to consider the 340°C data point a significant result.

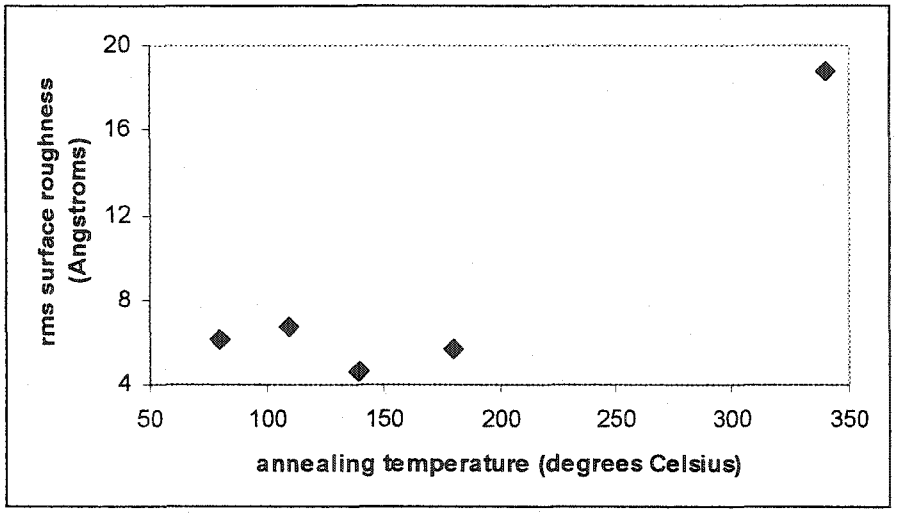

Fig. 5.7. A plot of the rms surface roughness versus post-deposition annealing temperature

Surface roughness is determined by two important mechanisms which act during the annealing process. One is surface diffusion, which is the dominant mechanism that smoothes surface features at low annealing temperatures. The other is the grain coarsening (Porath et al. 1994), which becomes dominant at higher temperatures and may be due to a combination of grain-boundary and bulk diffusion. Higher temperature annealing seems to produce large 3D structures and these large grains bulging out from the surface are responsible for an increased rms roughness.

The surface with the largest (111) terraces was obtained at an annealing temperature of 340°C (fig. 5.6d). This is consistent with others (Golan et al., 1992, Chidsey et al., 1988), who reported that the morphology of gold films annealed at temperatures around 300°C approaches that of samples deposited at high temperature.

Let us now return to the film presented in fig. 5.6d. The 0.5 μm×0.5 μm STM image exhibits a number of screw dislocations (see arrow). The figure also illustrates the effects of surface diffusion of gold atoms. A strong anisotropy in the surface diffusion is observed and produces highly asymmetric terraces. Many elongated islands and holes are finger-like extending from the terrace edges. Similar topography was reported previously by Emch et al. (1989). They found the dimensions of these protrusions are often quantized in units of 65 Å, the 22 unit cell distance observed in the 22×√3 ("herringbone") reconstruction of the

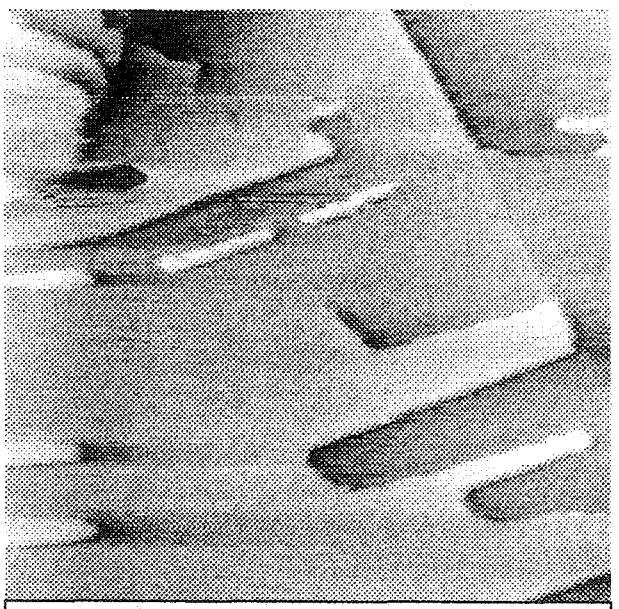

Figure 5.8. (2000Å×2000Å) image of an area of the surface illustrated in fig. 5.5d), exhibiting the characteristic 22×√3 reconstruction.

Au(111) surface. In other words, many of the structures are driven by the surface reconstruction. Indeed, our own data revealed that the surface is reconstructed. Fig. 5.8 presents a 2000Å×2000Å image of an area of the same film presented in fig. 5.6d. The image shows that the surface has undergone reconstruction and

the "herringbone" pattern is easily identifiable as alternating light and dark straight stripes, which occasionally exhibit 120° turns.

*

Having found the optimal annealing temperature, we studied the time dependence of annealing at this temperature. Freshly evaporated gold films were annealed for periods of time of between 1 and 12 h. The samples were then

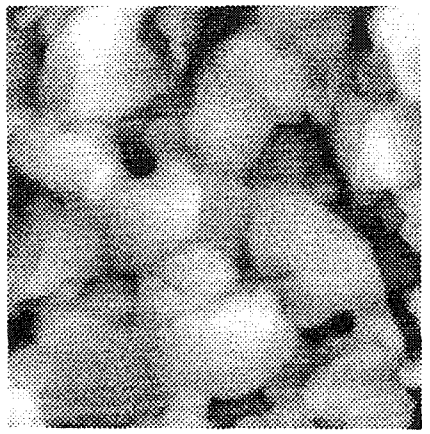

a) t = 0 h

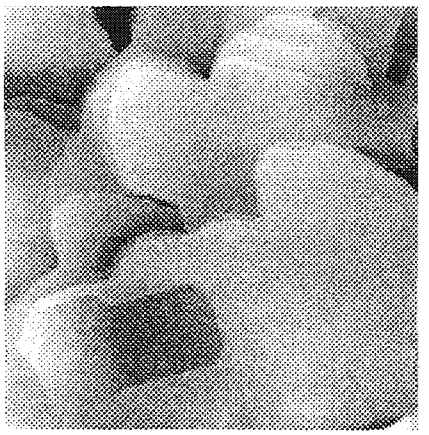

b) t = 1 h

c) t = 3 h 30 min

Figure 5.9. A sequence of 0.5 μm×0.5 μm STM images of gold films, one as -deposited, and two annealed immediately after deposition, at 340°C, for different periods of time.

Rms surface roughness values:
a) 13.5 Å; b) 2.26 Å; c) 18.8 Å

allowed to cool to ~30°C before exposing them to air. Fig. 5.9 gives a qualitative presentation of the changes in surface morphology with annealing time. Three 0.5 μm×0.5 μm STM topographic images of gold films evaporated on mica substrates held at room temperature are presented. One image was taken right after deposition (5.9a) with no post-annealing, and the other two were taken after annealing at 340°C for 1 h (5.9b), and 3 h 30 min (5.9c) respectively after deposition. Visual inspection reveals that post-deposition thermal treatment has the effect of significantly enlarging of the grains and enhancing of the (111) texture. Before annealing, the surface consisted of large flat hexagonal-shaped grains, along with smaller spherical grains occasionally clustered in groups of two or three (fig.5.9a). These initial features disappeared completely, even after one hour (5.9b), and very large and smooth grains developed. Consistent with our findings, Watanabe et al. (1991) reported that structural changes were more drastic in the early stages of the annealing process. The density of steps on top of the plateaus increased with annealing time (5.9b and c).

The trend in the evolution of rms surface roughness over time can be explained considering the mechanisms that take place during the annealing process. Initially surface diffusion leads to a reduction in the surface roughness during annealing at 340°C. With prolonged annealing, the surface roughness increases. Similar results were reported by Marchon et al., 1987, and may be driven by thermodynamics if the low energy configuration favors 3 D film structure.

*

With the last set of experiments, we tried to imitate the popular technique of *ex-situ* flame annealing which many people use as the preferred method of producing large crystalline domains. To mimic this step *in-situ,* we began by increasing the temperature rapidly to a predetermined value at which point the heating was terminated and the sample cooled rapidly. The flashing temperature was varied between 300 and 650°C. Above 650°C the samples deteriorated, apparently because of gold re-evaporation and disintegration of the mica substrate (Holland-Morritz, 1991, deRose et al., 1991).

Fig. 5.10 shows a series of gold films flash-annealed at different temperatures. As seen in fig. 5.10a) (the poor quality of this image is due to STM tip instability),

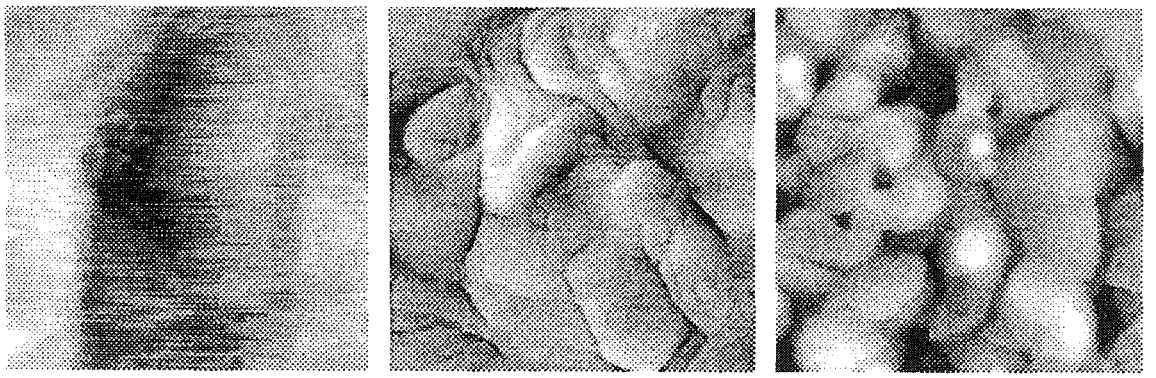

a) T = 650°C **b) T = 450°C** **c) T = 300°C**

Figure 5.10. A sequence of 0.5 μm×0.5 μm STM images of gold films flash-annealed at different temperatures.

Rms surface roughness values: a) 5.87 Å; b) 6.89 Å; c) 6.97 Å

at a flash heating temperature of 650°C, the gold grains are very crystalline and (111) terminated. Moreover, the islands on the surface have the triangular facets usually observed on single crystals. Dishner et al. (1998) obtained similar results,

when flame annealing in air gold films deposited at a substrate temperature of 380°C.

STM imaging showed that the triangular islands do not develop at lower annealing temperatures (figs. 5.10b). We found that flashing at temperatures below 350°C had no significant effect on the sample. The visual appearance of the film flashed at 300°C (fig. 5.10c) is similar to that of as-grown films.

There was no clear trend in the rms surface roughness values for the flash-annealed films, hence no conclusion regarding the effect of flash-heating on the roughness of films could be drawn. However, the smoothest film was the one annealed at 650°C.

We could explain, from a thermodynamic standpoint, why in annealed samples, islands tend towards a triangular shape as opposed to hexagons as follows: when gold grows epitaxially on a surface with at least threefold symmetry (such as mica), it will normally grow in its face-centered cubic structure with the (111) surface parallel to the substrate. A (111) layer is a hexagonal lattice so the gold islands tend to be hexagons, as seen in the films deposited at room temperature, before any thermal treatment (for instance, in fig. 5.1d). This yields close-packed island edges with relatively few high-energy atomic sites. However, it is generally true of fcc (111) growth that the hexagons are not equilateral, because three of the island edge directions are different in structure from the other three. One can see this by stacking balls. Building up a 3-D island from multiple layers, one finds that three edge directions develop into the <100> faces (100), (010), and (001), while the other three develop into the <111> faces $(\bar{1}11)$, $(1\bar{1}1)$ and $(11\bar{1})$.

Because of the different geometric structure, the energy per unit length is different for the two kinds of island edge. Thus the relative lengths will be different. In some cases one edge has a high enough energy that islands are nearly triangular, while in other cases they look like truncated triangles. This justifies a tendency toward triangular islands, especially after annealing. Annealing allows overcoming kinetic barriers and arising at a topography closer to equilibrium. In other words, annealing makes it possible to generate a more regular structure for the island shape and for the reconstruction. In both cases a threefold symmetry is preferred.

6. CONCLUSIONS

Many studies have been done on the system of gold of mica, and there are a considerable variety of proposed methods for the production of the highest quality gold films. The goal of the present work was to find the optimum conditions under which the gold films deposited on room temperature mica become crystalline. We were motivated primarily by the need to find convenient, flat substrates on which self-assembled monolayers could be observed with the STM.

The topography of the gold films, as revealed by STM imaging, was consistent with that reported in previous STM work done either in air or in UHV (Chidsey et al., 1988, Putnam et al., 1989, Watanabe et al., 1991): gold evaporation at rate of ~1 Å/s onto room temperature mica produces films that are comprised of large numbers of small grains of gold. Gold grains have an average size of about 220 Å and a preferred (111) texture.

Investigation of the influence of the mica pre-annealing time and the gold deposition rate on the surface structure allowed us to optimize the conditions for the formation of flat terraces. From the experimental results we were able to conclude that bake-outs of mica as long as 48 h or more, at a temperature of 340°C, and a deposition rate as low as 0.2 Å/s led to the preparation of gold films with large grains ~1000 Å wide.

Annealing of samples following deposition promoted further enlargement of grain size and enhancement of (111) texture. The evolution of the surface morphology as a function of annealing temperature and duration was studied. Annealing at

the same temperature as mica pre-annealing for 1 h produced the highest quality gold films.

We also used *in-situ* flash annealing as an innovative method to mimic the popular method of *ex-situ* flame annealing (Dishner et al. 1998). The *in-situ* method promises to be more controllable/reproducible than the flame anneal step. The optimum flashing temperatures were found to be between 500 and 650°C. Samples thus annealed exhibited very large gold terraces (many in excess of 5000 Å in width) with triangular shapes. Roughness of flashed films was dramatically decreased compared to as-deposited films, the smoothest film being obtained at a flashing temperature of 650°C. Flashed films also seemed to be smoother than all their annealed analogues, with the exception of the film annealed for 1 h.

In each of the experiments we did, we measured the rms surface roughness of the films. In the first set of experiments, grain size increased with mica pre-annealing, as did the roughness. In the next set, grain size increased with decreasing deposition rate but rms roughness decreased as well. When annealing follows growth, whether it is prolonged or flashing, rms roughness fluctuates, due to several competing things going on. As a result of these measurements, we strongly believe that using rms roughness as the sole measure of film quality can be misleading.

In conclusion, the optimized preparation conditions for gold films with the largest (111) terraces under the constraints of our experimental apparatus are: (1) a minimum vacuum pressure in the evaporator of 10^{-7} Torr; (2) a mica pre-

annealing period of about 48 h at 340°C; (3) a gold deposition rate of 0.2 Å/s; (4) subsequent to gold deposition: i) an annealing step at 340°C for 1 h, or ii) a flash-annealing treatment at 650°C. Under the above conditions it is possible to prepare films with typical grain sizes of ~ 3000 Å and rms surface roughness values of ~2 Å (for *i* above), or films with a typical grain size of at least 5000 Å and an rms roughness of ~ 6 Å (for *ii* above). These high quality thin films of pure (111)-terminated gold are most suitable for SAM studies.

REFERENCES

Adamsky, R. F., Nucleation and Growth of Metal Films (p.243), in *Use of Thin Films in Physical Investigations* (Editor J. C. Anderson), Academic Press, London and New York, 1966

Bardeen, J., Phys. Rev. Lett. **6** (2) (1960) p. 57-59

Bartelt, M.C., and Evans, J.W., Phys. Rev. B **46**, 12 675 (1992)

Besocke, K., Surface Science **181** (1987) 145-153

Binnig, G., Rohrer, H., Gerber, Ch., Weibel, E., Phys. Rev. Lett. **49** vol.1 (1982) 57-61

Bonnell, Dawn A, *Scanning Tunneling Microscopy and Spectroscopy (Theory, Techniques and Applications)*, VCH Publishers Inc., 1993

Bruck, L., Ann. Phys., Leipzig, **26** (1936) p. 233

Buchholz, S., Fuchs, H., and Rabe, J.P., J. Vac. Sci. Technol. B **9** (2) (1991) 857-861

Campbell, D.S., Methods of Preparing Thin Films (p.11), in *The Use of Thin Films in Physical Investigations* (ed. J.C. Anderson), Academic Press, London and New York, 1966

Chidsey, C.E.D., Loiacono, N., Sleator, T, Nakahara, S., Surface Science **200** (1988) 45-66

De Rose, J.A., Thundat, T., Nagahara, L.A., and Lindsay, S.M., Surface Science **2** (1991) 102-108

De Vries, J.W.C., J.Phys. F **17**, (1987) 1945-1952

Dishner, M.H., Hemminger, J.C., and Feher, F.J., Langmuir **1997**, *13*, 2318-2322

Dishner, M.H. , Ivey, M., Gorer, S., Hemminger, J.C., and Feher, F.J., J. Vac. Sci. Technol. A **16**(6), (1998), 3925-3300

Elliot, A. G., Surface Science **44** (1974) 337-359.

Emch, R., Nogami, J., Dovek, M.M., Lang, C.A., and Quate, C.F, J. Appl. Phys. **65** (1) (1989) 79-83

Ferguson, Ian, *Auger Microprobe Analysis*, IOP Publishing LTD, Bristol, England, 1989

Francombe, M. H., The Preparation of Epitaxial Films by Evaporation and Cathodic Sputtering (p.29), in *Use of Thin Films in Physical Investigations* (Editor J. C. Anderson), Academic Press, London and New York, 1966.

Golan, Y., Margulis, L., and Rubinstein, I., Surface Science **264** (1992) 312-326

Hallmark, V.M., Chiang, S., Rabolt, J.F., Swalen, J.D., and Wilson, R.J., Phys. Rev.Lett. **59** (1987) 2879

Harris, A., J. Appl. Phys. **39**, (1968) 1419-1428

Harsdorff, M., and Raether, H., Z. Naturf. *A* **19** (1964) p. 1497

Hazen R. M., Finger L. W., Velde D., American Mineralogist **66** (1981) 586-591

Heavens, O. S., Thin Film Physics, Methuen, London, 1971.

Hedberg, C.A., *Handbook of Auger Electron Spectroscopy*, 3rd edition, Physical Electronics, Eden Prairie Mn., 1995

Hemminger, John C., private communication (2002)

Holland, L., *Vacuum Deposition of Thin Films*, Chapman & Hall, London, 1956

Holland-Moritz, E., Gordon, J., Borges, G., Sonnenfeld, R., Langmuir **1991** *7*, 301-306

Ino, S., et al., J.Phys.Soc, Japan, **17**, 1074 (1962)

Ino, S., et al., J.Phys.Soc, Japan, **19**, 881 (1962)

Kern, R., Le Lay, G., and Metois, J.J., Basic Mechanisms in the Early Stages of Epitaxy. In *Current Topics in Materials Science* (ed. E. Kaldis), vol.**3**, Chapter 3, Amsterdam: North-Holland, 1979

Lander, J.J., Phys. Rev. **91** (1953) 1382

Lang, C.A., Surface Science **224** (1989) L947-L955

Lin, T.-S, and Chung, Y.-W., Surface Science **207** (1989) 539-546

Lüth, Hans, *Surfaces and Interfaces of Solids*, second edition, Springer-Verlag New York Berlin Heidelberg, 1993

Marchon, B., Ferrer, S., Kaufman, D.S., and Salmeron, M., Thin Solid Films **154** (1987) 65-73

Matthews, J.W., Phil. Mag. **7** (1962) 915

Matthews, J.W., Phil. Mag. **10** (1965) 815

O'Hanlon, John F., *A User's Guide to Vacuum Technology*, 2nd Ed., John Wiley &Sons, Inc., Toronto, 1989

Ohring, Milton, *The Materials Science of Thin Films*, Academic Press, Inc., San Diego, 1992

Pashley, D.W., et al., Phil. Mag.**10** (1964), p.127

Pashley, D.W., Advanc. Phys. **14** (1965) 327

Pashley, D.W., Advanc. Phys. **5** (1956) 173

Poppa, Helmut, Heinemann, K., and Elliot, A.G., J. Vac. Sci. Technol **8** no.3 (1970) 471-480

Porath, D., Goldstein, Y., Grayevsky, A., and Millo, O., Surface Science **321** (1994) 81-88

Prutton, M., *Introduction to Surface Physics*, Oxford University Press Inc., New York, 1994

Putnam, A., Blackford, B.L., Jericho, M.H., and Watanabe, M.O., Surface Science **217** (1989) 276-288

Reichelt, K., Lutz, H.O., Journal of Crystal Growth **10** (1971) 103-107

Rhodin, T.N., and Walton, D., Nucleation of Oriented Films (p.31) in *Single Crystal Films*, edited by M.H. Francombe and H. Sato (Oxford: Pergamon Press), 1964

Rhodin, T.N., Nucleation and Growth on Solid Surfaces (p.187): Theory and Application, in *Use of Thin Films in Physical Investigations* (edited by J. C. Anderson), Academic Press, London and New York, 1966.

Salmeron, M., Kaufman, D.S., Marchon, B., Ferrer, S., Applied Surface Science **28** (1987) 279-290

Smith, T., Journal of Colloid and Interface Science **75**, No.1, (1980) 51-55

Spânulescu, I., Physics of thin films and their applications, Scientific Publishing House, Bucharest, 1975

Tersoff, J., Hamann, D.R., Phys Rev. B **31** (1985) 805

Tersoff, J., Hamann, D.R., Phys Rev.Lett **50** (1983) 1998

Van der Merwe, J.H., *Recent Developments in the theory of epitaxy*, in Chemistry and Physics of Solid Surfaces V, eds. Vanselow and Howe, Berlin: Springer-Verlag (1984) 365-401

Vancea, J., Reiss, G., Schneider, F., Bauer, K., and Hoffmann, H., Surface Science **218** (1989) 108-126

Venables J.A., Spillert, G.D.T, and Hanbucken, M., *Nucleation and Growth of thin films*, Rep. Prog. Phys, Vol **47** (1984) 399-459,

Venables, J.A. and Price, G.L., *Nucleation of Thin Films*, in Epitaxial Growth Part B, published by Academic Press Inc. (London), 381-432, 1975

Venables, J.A., *New Experimental Approaches to Studies of Nucleation and Growth on surfaces*, in Current Topics in Materials Science vol.2, ed. E. Kaldis, North-Holland Publishing Company, 1977

Venables, J.A., *Introduction to Surface and Thin Film Processes*, Cambridge University Press, 2000

Volmer, M., Weber, A., Z. Phys. Chem. **119** (1926) 277

Wagner, T., High Temperature Epitaxial Growth and Structure of Nb Films on α-Al_2O_3(0001), Journal of Materials Research **13** (1998) p.693.

Watanabe, M. O., Kuroda, T., Tanaka, K., and Sakai, A., J. Vac. Sci. Technol. B **9** (2) (1991) 924-927

Wang, Z., and Moskovits, M., Journal of Applied Physics **71** (1992), p.5401-5409

Witt, G. R., The Electromechanical Properties of Thin Films and the Thin Film Strain Gauge, Thin Solid Films **22** (1974) p.133-156.

Zangwill, Andrew, *Physics at Surfaces*, Cambridge University Press, Great Britain, 1988